

Cell cycle regulation has shaped replication origins in budding yeast

Received: 16 January 2025

Accepted: 15 May 2025

Published online: 30 June 2025

 Check for updates

Chew Theng Lim^{1,7}, Thomas C. R. Miller^{2,3,7}✉, Kang Wei Tan¹,
Saurabh Talele^{4,5}, Anne Early¹, Philip East⁶, Humberto Sánchez⁴,
Nynke H. Dekker^{4,5}, Alessandro Costa² & John F. X. Diffley¹✉

Eukaryotic DNA replication initiates from genomic loci known as origins. At budding yeast origins like ARS1, a double hexamer (DH) of the MCM replicative helicase is assembled by origin recognition complex (ORC), Cdc6 and Cdt1 by sequential hexamer loading from two opposed ORC binding sites. Cyclin-dependent kinase (CDK) inhibits DH assembly, which prevents re-replication by restricting helicase loading to the G1 phase. Here, we show that an intrinsically disordered region (IDR) in the Orc2 subunit promotes interaction between ORC and the first loaded, closed-ring MCM hexamer (the MCM–ORC (MO) intermediate). CDK-dependent phosphorylation of this IDR blocks MO formation and DH assembly. We show that MO stabilizes ORC at lower-affinity binding sites required for second hexamer loading. Origins comprising two high-affinity ORC sites can assemble DH efficiently without MO by independently loading single hexamers. Strikingly, these origins escape CDK inhibition *in vitro* and *in vivo*. Our work reveals mechanistic plasticity in MCM loading with implications for understanding how CDK regulation has shaped yeast origin evolution and how natural, strong origins might escape cell cycle regulation. We also identify key steps common to loading pathways, with implications for understanding how MCM is loaded in other eukaryotes.

The initiation of eukaryotic DNA replication is separated into two temporally distinct steps that ensure no region of the genome is replicated more than once^{1–3}. During the G1 phase, a pair of hexameric MCM helicases is loaded at each replication origin around double-stranded DNA in the form of a head-to-head MCM–DH. During S-phase, each DH is converted into two active CMG (Cdc45–MCM–GINS) helicases, thereby initiating bidirectional DNA replication.

Budding yeast DNA replication origins generally contain a high-affinity ORC binding site flanked by one or more low-affinity sites in the opposite orientation^{4–6}. At ARS1 (Fig. 1a), the bipartite high-affinity site comprises the A and B1 elements (A/B1), and a lower-affinity site corresponds to the B2 element^{6–8}. Both the A and B2 elements contain

the extended ARS consensus sequence (EACS); the A element is a closer match to the EACS than B2. DH assembly at ARS1 occurs by sequential loading of two MCM hexamers (outlined in Fig. 1b)^{5,9,10}. After loading of the first hexamer (Fig. 1b(i–iii)), ORC releases from A/B1. ORC then binds both B2 and the amino-terminal domain of the first loaded MCM, generating the ‘MO’ complex (Fig. 1b(iv))¹¹. The same ORC that was bound to A/B1 can ‘flip’ and bind B2 (ref. 12); alternatively, a second ORC molecule can bind B2 and engage the first recruited MCM (ref. 5). In MO, the MCM ring is closed and MCM subunits are primarily in a post-hydrolysis (ADP-bound) state, very similar to the DH¹¹. Given that this second ORC binding event also induces a DNA bend, the face of ORC that promotes initial MCM recruitment and ORC–Cdc6–Cdt1–MCM

¹Chromosome Replication Laboratory, The Francis Crick Institute, London, UK. ²Macromolecular Machines Laboratory, The Francis Crick Institute, London, UK. ³Center for Chromosome Stability, Department of Cellular and Molecular Medicine, University of Copenhagen, Copenhagen, Denmark.

⁴Department of Bionanoscience, Kavli Institute of Nanoscience, Delft University of Technology, Delft, The Netherlands. ⁵Department of Physics and Kavli Institute of Nanoscience Discovery, University of Oxford, Oxford, United Kingdom. ⁶Bioinformatics & Biostatistics, The Francis Crick Institute, London, UK.

⁷These authors contributed equally: Chew Theng Lim, Thomas C. R. Miller. ✉e-mail: tmiller@sund.ku.dk; john.diffley@crick.ac.uk

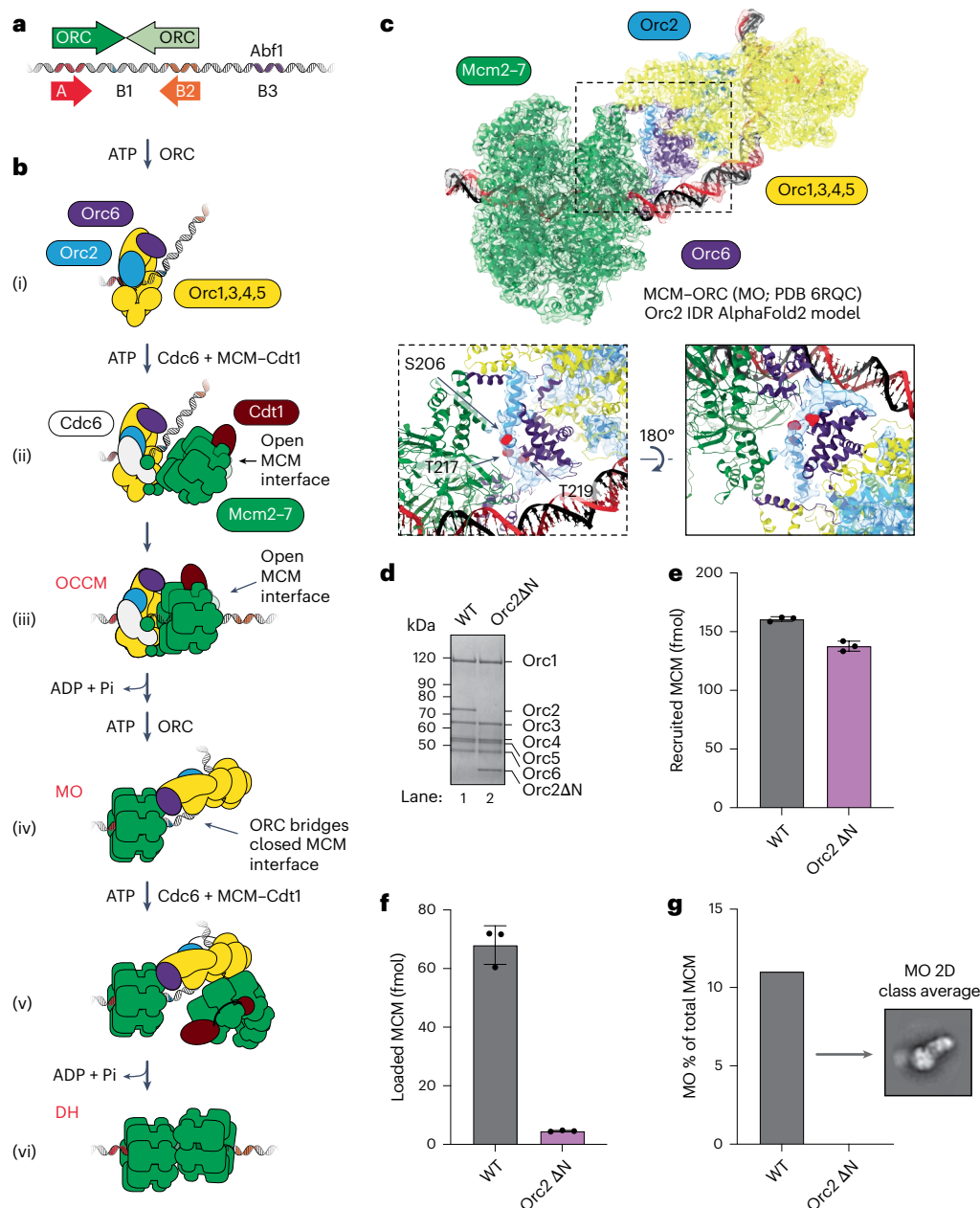


Fig. 1 | The Orc2 IDR is a key element of the MCM-ORC interface. **a**, Architecture of the canonical ARS1 origin of replication, with high-affinity (dark green) and low-affinity (light green) ORC binding sites. **b**, Schematic of the DH formation pathway: (i) ORC binds an A/B1 element and bends the DNA. (ii) ORC recruits a first MCM hexamer and (iii) threads DNA through the open Mcm2-5 gate, forming an OCCM intermediate. (iv) ATP hydrolysis promotes OCCM disassembly and first MCM loading. ORC is released from A/B1, and an ORC binds to both the B2 and the N-terminal face of the first loaded MCM, forming an MCM-ORC ('MO') complex. ORC recruits (v) and then loads (vi) a second MCM onto the origin, forming a DH. **c**, Cryo-EM structure of the MCM-ORC intermediate (PDB 9I31, EMD-4980 (ref. 11)), including the Orc2 IDR (amino acids 190-231) modeled by AlphaFold2 (ref. 14). The Orc2 IDR, including CDK phosphorylation sites

S206, T217 and T219, occupies previously unassigned EM density at the center of the MCM-ORC interface (see dotted insert on left and a 180° rotated view on the right). The Orc2 EM density has been isolated from a density-modified (EMready⁴⁵) map of ORC obtained from the multibody refinement of the MO¹¹. **d**, Orc2ΔN is stably incorporated into the ORC complex. **e**, DNA-pulldown assays show Orc2ΔN recruits luciferase-tagged MCM to ARS1 in ATPγS with comparable efficiency to WT ORC. **f**, Orc2ΔN is compromised in MCM loading on ARS1 in ATP. The data in (e) and (f) are plotted as means of three technical replicates; error bars, s.d. **g**, MCM loading assays visualized by negative-stain EM show that Orc2ΔN fails to form MO on ARS1. Quantification of micrographs, total MCM and MO in negative-stain EM 2D classification data: WT (156, 6,159, 680); Orc2ΔN (167, 5,733, not detected).

(OCCM) formation is available in MO to receive the second MCM-Cdt1 without steric interference (Fig. 1b(v)). MO is thus poised to be a key intermediate in DH assembly (Fig. 1b(vi)); nonetheless, the exact mechanism of MO formation, its function and its importance in DH assembly remain unclear. Moreover, whether all DH assembly proceeds via MO is unknown.

CDKs have a crucial role in ensuring that replication occurs only once per cell cycle by inhibiting DH assembly outside of the G1 phase.

They do so by promoting proteasome-dependent degradation of Cdc6 and nuclear exclusion of MCM-Cdt1. They also inhibit DH assembly directly by phosphorylation of the ORC subunits Orc2 and Orc6 (refs. 1-3). Single-molecule experiments have recently indicated that Orc6 phosphorylation promotes premature release of MCM-Cdt1, while stable MCM ring closure around DNA and MO formation do not occur efficiently after phosphorylation of Orc2 or Orc6 (ref. 13).

Results

MO is crucial for MCM loading at ARS1

We first sought to understand the importance and role of MO in DH assembly by identifying an ORC mutant that cannot form MO. We have previously shown that an N-terminal deletion of the Orc6 subunit of ORC (Orc6 Δ 119) reduced both MO and DH formation by approximately 50%, consistent with the idea that MO is a precursor of DH¹¹; however, this was a relatively modest effect, and we wanted to generate a mutant with more complete loss of MO formation. Orc2 contains a long (235 amino acid) N-terminal extension that is predicted by AlphaFold¹⁴ to be intrinsically disordered. The Orc2 IDR has not been resolved in any ORC structure determined experimentally, including MO. A region of the Orc2 IDR was tentatively assigned as wrapping around Orc6 in a cryogenic electron microscopy (cryo-EM) density map of DNA-bound ORC¹⁵, albeit at a resolution that prevented assignment of the amino acid sequence and inclusion of this region in the entry deposited in the Protein Data Bank (PDB 5ZR1 (ref. 15)). Using AlphaFold2 multimer¹⁶, we identified a region of the Orc2 IDR docking on the carboxy-terminal domain of Orc6 with high confidence (Fig. 1c and Extended Data Fig. 1), consistent with the density seen in that previous work¹⁵. Notably, overlaying our AlphaFold prediction with our previously determined structure of the MO intermediate places the region of the Orc2 N-terminal IDR (amino acids 190–231) into a contiguous stretch of density at the core of the MCM–ORC interface, suggesting that it may have a key role in MO formation (Fig. 1c). Deletion of this IDR from Orc2 did not affect the ability of Orc2 to form a stable complex with the other ORC subunits (Fig. 1d). ORC complexes containing this deletion (Orc2 Δ N) recruited MCM normally in ATPyS (Fig. 1e). However, Orc2 Δ N loaded MCM at a level only 7% that of wild-type (WT) ORC (Fig. 1f). To visualize the effect of Orc2 IDR truncation on DH formation directly, we performed MCM loading assays on a 454 bp linear DNA template containing ARS1 flanked by nucleosomes and imaged the reactions by negative-stain EM. Although MO was readily detectable with WT ORC in ATP, consistent with previous work¹¹, MO was not detected in reactions with Orc2 Δ N (Fig. 1g). These experiments show that the Orc2 IDR is essential for forming the MO intermediate, and that the inability to form MO compromises DH assembly, indicating that MO is a crucial intermediate in the assembly of the DH at ARS1. Small amounts of DH assembly by Orc2 Δ N suggest the existence of an inefficient, MO-independent DH assembly pathway at ARS1.

MO is required to stabilize ORC at weak binding sites

The two key ORC binding sites at ARS1 (A/B1 and B2) are so close together that ORC cannot bind both sites simultaneously⁶. Therefore, MCM loading must occur in two sequential ORC binding steps. As shown in Fig. 2a, we arranged budding yeast origins according to the distance between the best match to the EACS (A domain) and the best predicted secondary ORC site in the opposite orientation (B2-like domain). In roughly one-third of yeast origins, the two ORC binding sites are as close or closer together than A/B1 and B2 in ARS1 (Fig. 2a). Using synthetic origins with two high-affinity ORC sites (perfect EACS/B1) in which distances are measured from the inside edges of the two B1 elements, 10 bp corresponds to the distance between A/B1 and B2 in ARS1, and this construct, like ARS1, can only bind a single ORC molecule (Extended Data Fig. 2a, lanes 5 and 6). Moving binding sites just 2 bp farther apart, however, allows two ORC molecules to bind simultaneously (Extended Data Fig. 2a, lanes 7 and 8). Thus, roughly two-thirds of yeast origins are predicted to allow simultaneous binding of two ORC molecules (Fig. 2a), unlike ARS1. In approximately 20% of yeast origins, the two predicted ORC binding sites are far enough apart to fit a single MCM hexamer between them, and in 23%, they are far enough apart to fit a DH between them. In only 15% of origins is the weaker ORC binding site a better EACS match than ARS1 B2 (Extended Data Fig. 2b). Therefore, asymmetry in ORC binding affinities appears to be a general property of yeast origins regardless of whether or not the two sites overlap. The

MCM loading mechanism has primarily been studied using ARS1; it remains unclear whether the mechanism of MCM loading is the same at all origins or whether other mechanisms may be important at origins with different ORC binding affinities or wider spacing between ORC binding sites.

To begin to address this question, we tested the ability of Orc2 Δ N, which cannot form MO at ARS1, to load MCM on a series of synthetic origins with two high-affinity ORC binding sites in the opposite orientation, placed at distances 10–300 bp apart. As shown previously⁵, WT ORC can load MCM efficiently on this series of origins, with a peak of MCM loading at 70–90 bp, but with efficient loading even at 300 bp. Orc2 Δ N cannot load MCM efficiently at ARS1, but surprisingly, loads MCM at all distances from 10–300 bp as efficiently as WT ORC (Fig. 2b). To determine whether Orc2 Δ N can promote MO formation in the context of origins with two high-affinity ORC binding sites, we performed cryo-EM on early time-point (2 min) MCM loading reactions with either WT ORC or ORC containing Orc2 Δ N using the 90 bp synthetic origin. Although MO particles were amongst the most abundant single hexamer (SH)-containing particles with WT ORC, they were not detected with Orc2 Δ N, even though similar numbers of DHs were detected (Fig. 2c and Extended Data Fig. 3), consistent with the biochemical data. Approximately 3 Å resolution structures of DHs, formed with WT ORC and Orc2 Δ N, appear identical (Extended Data Fig. 3). Moreover, DHs formed on the 90 bp origin with Orc2 Δ N are fully competent to support replication with purified proteins (Fig. 2d). Therefore, Orc2 Δ N cannot form MO, even on a template with two high-affinity sites, but can load functional DHs very efficiently. This shows that MO is not required when MCM is loaded from two high-affinity sites, regardless of whether those sites effectively overlap (10 bp) or are separated by a relatively large distance (300 bp). To test this concept directly, we changed one high-affinity EACS/B1 site in the most efficient synthetic template (90 bp) to the B2 element from ARS1, a lower-affinity ORC site (Fig. 2e). As shown in Fig. 2f, WT ORC loads MCM as efficiently on this template as it does on the parent template with two high-affinity sites, demonstrating that weak ORC sites can be effectively used even when the two ORC sites do not overlap. MCM loading with Orc2 Δ N on the 90 bp template was at least as efficient as WT, but MCM loading on the 90bp-B2 construct was greatly reduced. From these experiments, we conclude that the MO intermediate is critical for MCM loading when one of the ORC binding sites is of lower affinity, and, therefore, that the essential role of MO in DH assembly is to stabilize ORC binding at weak sites after first hexamer loading. Furthermore, MO is still essential when the high-affinity and low-affinity ORC sites are 90 bp apart, indicating that MO is not just required when ORC sites overlap, as in ARS1. However, MO is not required when MCM is loaded from two high-affinity ORC binding sites.

Given that the EACS/B1 sequences in both 90 bp and 90bp-B2 are high-affinity ORC binding sites, ORC binding to these sequences is stable under stringent (150 mM NaCl) washing, whereas binding to B2 is not⁵, which allows us to examine the efficiency of the ‘one ORC’ loading via ORC flipping versus the two ORC MO-independent mechanism in which a second ORC molecule loads the second hexamer. To test this concept, we pre-bound different concentrations of ORC to either the 90 bp or the 90bp-B2 origin; free ORC along with B2-bound ORC was then washed off (Extended Data Fig. 2c). Under these conditions, ORC remains stably bound to the high-affinity EACS/B1 element in both templates in the presence of excess competitor DNA for at least 60 min (Extended Data Fig. 2d). Finally, we added Cdc6 and MCM–Cdt1 and examined MCM loading. MCM loading under these conditions on the 90bp-B2 origin defines the maximal efficiency of MCM loading from a single ORC molecule. At saturating ORC concentrations, all binding sites in the 90 bp origin are bound, so there are no free binding sites for ORC to flip onto after first hexamer loading, and, therefore, all loading must occur via two ORC molecules. That this loading does not occur via the MO-dependent pathway is supported by the fact that Orc2 Δ N is as

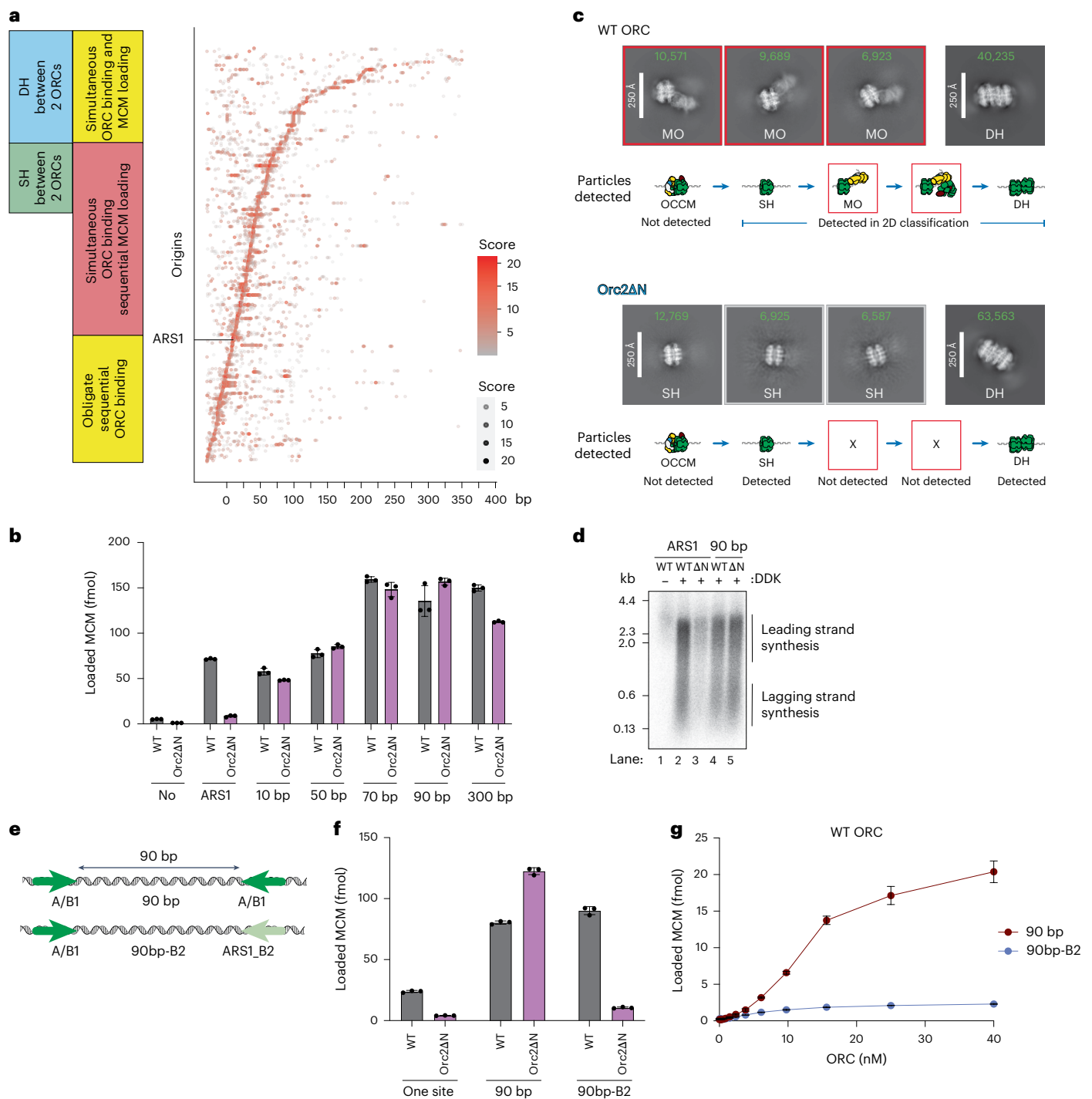


Fig. 2 | The MO promotes MCM loading by stabilizing ORC at low-affinity binding sites. a, Matches to the EACS were identified using a position weight matrix (PWM) as previously described⁵. Origins are arranged according to the distance between the center of the best match to the EACS and the center of the best B2-like EACS by PWM in the opposite orientation. PWM scores are indicated by the size and color of dots, as indicated in the figure. **b**, Orc2ΔN loads MCMs onto origins containing two high-affinity inverted ORC binding sites spaced ≥ 10 bp apart with comparable affinity to WT ORC. The data are plotted as means of three technical replicates; error bars, s.d. **c**, Cryo-EM 2D classification of early time-point MCM loading assays showing that Orc2ΔN cannot form MO intermediates on 90 bp origins containing symmetrical high-affinity ORC binding sites. Green numbers indicate the number of particles contributing to each class average. Total micrographs analyzed (WT, 18,156; Orc2ΔN, 18,414); total particles containing single MCM helicases (WT, 188,324; Orc2ΔN, 244,701);

and total particles containing MCM-DHs (WT, 149,543; Orc2ΔN, 137,314). The top three (SH-containing) or one (DH) classes are shown; the full classification is shown in Extended Data Fig. 3. **d**, MCMs loaded onto 90 bp origins by WT ORC and Orc2ΔN are replication competent. **e**, Schematic of synthetic origins containing inverted high-affinity ORC binding sites spaced 90 bp apart (top), or with one high-affinity site replaced by the ARS1 B2 element (bottom). **f**, MCM loading on 90 bp origins by Orc2ΔN is dependent on two high-affinity ORC binding sites. The data are plotted as means of three technical replicates; error bars, s.d. **g**, MCM loading by WT ORC, showing two DNA-bound ORCs load MCM more efficiently than one ORC at various concentrations. ORC was preincubated with DNA beads and washed twice with LSW + 150 mM NaCl buffer. Cdc6 and MCM-Cdt1 were then added to the reaction and incubated for another 5 min. The data are plotted as means of three technical replicates; error bars, s.d.

efficient as WT ORC at MCM loading from the two-site template under these conditions (Extended Data Fig. 2e). By contrast, loading on the 90bp-B2 template is strongly reduced with Orc2 Δ N (Fig. 2f) and, under the staged conditions, increases only linearly with increasing ORC concentration (Fig. 2g). As shown in Fig. 2g, there was approximately tenfold more loading on 90 bp than 90bp-B2 at high ORC concentrations. This result is consistent with the idea that a single ORC can load a DH from a single high-affinity site via ORC flipping and MO formation, but also shows that this pathway is less efficient than the pathway in which each MCM-SH is loaded by separate ORC molecules at two high-affinity sites. We note that at low ORC concentrations (<5 nM), loading on 90 bp and 90bp-B2 is similar. At these concentrations, loading on 90 bp is also predominantly via the one-ORC pathway, suggesting that B2 works as well as EACS/B1 as the second site in this pathway, consistent with the idea that MO stabilizes ORC binding to the weaker B2 site. These experiments imply that once the first hexamer is loaded, some subsequent step(s) in the one ORC mechanism—ORC release from A/B1, SH sliding away from B2, ORC rebinding B2 or second hexamer loading from the MO complex—have some inherent inefficiency. Taken together, we distinguish three separate ways MCM can be loaded: one ORC via MO, two ORC via MO and two ORC MO-independent.

CDK phosphorylation of Orc2 blocks MO formation

CDK prevents MCM loading outside of the G1 phase by promoting Cdc6 proteolysis^{17–20} and MCM–Cdt1 nuclear export^{21–25} as well as by inhibiting the ability of ORC to assemble DHs^{26–28}. The region in the Orc2 IDR predicted to form part of the MCM–ORC interface in MO (Fig. 1c and yellow box in Extended Data Fig. 4) is moderately conserved among closely related budding yeasts, which all contain multiple potential CDK phosphorylation sites near the predicted interface with MCM in MO (Fig. 1c, red dots). Therefore, we reasoned that CDK phosphorylation of Orc2 might inhibit MCM loading by interfering with MO formation. Phosphorylation of WT ORC with S-phase CDK (Cib5–Cdc28–Cks1) caused a reduction in mobility of both the Orc2 and Orc6 subunits in SDS–PAGE (Fig. 3a); this CDK-phosphorylated ORC was very inefficient in DH formation at ARS1 (Fig. 3b), consistent with previous work^{26–28}. Similar to Orc2 Δ N, however, phosphorylated ORC loaded MCM almost as well as unphosphorylated ORC on the 90 bp synthetic origin (Fig. 3b). To ensure that this loaded MCM was functional, we tested its ability to support DNA replication in vitro with purified proteins. Although pre-phosphorylated ORC did not support replication from an ARS1-containing template (compare lanes 2 and 3 in Fig. 3c), it supported replication from a template containing the 90 bp origin almost as well as unphosphorylated ORC (lanes 4 and 5, Fig. 3c), indicating that the DH formed is functional. Consistent with this idea, a 2.8 Å resolution cryo-EM structure of DH assembled with phosphorylated ORC is virtually identical to DH assembled with unphosphorylated ORC (Table 1 and Extended Data Fig. 5a). To test whether this 90 bp origin could also bypass CDK regulation of ORC in vivo, we reasoned that we might see re-replication from this origin in cells where Cdc6 and Cdt1–MCM regulation by CDK was bypassed, leaving cells to rely on CDK regulation of ORC to prevent re-replication²⁹. Bypassing Cdc6 and Cdt1–MCM regulation is necessary because even in the MO-independent pathway, Cdc6 and Cdt1 are required for SH loading. We used a yeast strain in which CDK regulation of MCM was constitutively eliminated by fusing an unregulated nuclear localization sequence (SV40-TAG NLS) to Mcm7, and CDK regulation of Cdc6 was conditionally deregulated with a copy of a stable version of Cdc6 (Cdc6 Δ NT) under a galactose-inducible promoter. When both Cdc6 and MCM are deregulated, cells rely entirely on WT ORC phosphorylation to prevent re-replication²⁹. We integrated a series of origins in place of ARS419, then arrested cells in G2/M, expressed stable Cdc6 and examined copy number after 3 h. As shown in Fig. 3d, deregulation of Cdc6 and MCM did not lead to any increase in DNA copy number of ARS1; ARS317, which had been previously shown to re-replicate under

similar conditions³⁰, showed elevated copy number, but the 90 bp origin showed the largest increase in copy number after Cdc6 deregulation, consistent with the idea that this synthetic origin bypasses CDK regulation of ORC both in vitro and in vivo.

We next sought to determine which step in DH assembly was blocked by Orc2 phosphorylation. To examine the effects of Orc2 phosphorylation alone, we mutated four serine/threonine residues in the CDK consensus sequences (^{S/T}/PX^{K/R}) in Orc6 to alanine to generate Orc6-4A. As shown in Fig. 3a, the phosphorylation-dependent shift of Orc6 was greatly reduced in Orc6-4A, but Orc2 was still shifted by CDK phosphorylation. On ARS1, CDK phosphorylation of Orc2 did not affect MCM recruitment in ATP γ S (Fig. 3e). However, Orc2 phosphorylation led to a substantial reduction in DH formation in both DNA-pulldown (Fig. 3f(i)) and EM-based (Fig. 3f(ii)) assays and a complete inhibition of MO formation (Fig. 3g), indicating that phosphorylation of Orc2 alone is sufficient to inhibit DH formation. Thus, CDK phosphorylation of Orc2, like deletion of the Orc2 IDR (Fig. 1), inhibits DH assembly before MO formation, consistent with recent work¹³. Although CDK phosphorylation of Orc2 blocks MO formation and DH formation on the ARS1 origin, it does not block DH formation on the 90 bp origin (Fig. 3b), consistent with the results in the previous section showing that MO is not required when origins contain two high-affinity binding sites (Fig. 2b,f).

Structure of the MCM-SH

Formation of MO requires Orc2 and Orc6 to bridge the N-terminal interface between the Mcm2 and Mcm5 subunits that form MCM's DNA entry 'gate'. However, it is currently unknown whether closure of the Mcm2–5 interface precedes ORC binding in the MO or whether ORC binding closes the Mcm2–5 gate to load the first MCM hexamer. Phosphorylated Orc2 (Orc6-4A) recruits MCM normally but does not form MO, suggesting that Orc2 phosphorylation either blocks a step in the loading of the SH (for example, OCCM disassembly) and/or directly prevents ORC binding to a loaded SH during the formation of MO. To investigate, we performed single-particle reconstitution in silico (ReconSil)¹¹ experiments to visualize entire chromatinized origins of replication during MCM loading reactions containing phosphorylated or truncated Orc2. ReconSil experiments enabled us to identify SHs that were apparently trapped on DNA between nucleosomes (Fig. 4a). Thus, the Orc2 IDR seems not to be required for OCCM assembly or disassembly to release SH onto DNA but is required for MO formation, which can be inhibited by CDK phosphorylation of the Orc2 IDR.

To confirm this idea, we used cryo-EM to visualize the helicase loading reaction with CDK-phosphorylated Orc2. The 3.4 Å resolution structure (3.1 Å after density modification) shows a single MCM ring encircling duplex DNA (Fig. 4b, Table 1 and Extended Data Fig. 5). Unlike the MCM in the OCCM structure, the SH contains a completely closed Mcm2–5 interface identical to that seen in the DH (Fig. 4b and Extended Data Fig. 5b). Thus, phosphorylation of ORC2 blocks DH formation after a SH has been fully closed around DNA, implying that ring closure precedes and is not a consequence of the N-terminal ORC binding that results in MO formation. Comparison with MCM in the OCCM complex reveals that the DNA grip in the helicase ring changes after closure of the Mcm2–5 gate (from Mcm7–4–6–2 to Mcm3–7–4–6 duplex engagement), probably as a consequence of ATP hydrolysis (Fig. 4b). Nucleotide occupancy changes from ATP γ S in the 3–7, 7–4, 4–6 and 6–2 interfaces in OCCM, to ATP in the 4–6 and 6–2 interfaces and ADP in the 2–5, 5–3, 3–7 and 7–4 interfaces in SH (Fig. 4c). This change in nucleotide occupancy indicates a minimum of four ATP hydrolysis events that may drive the re-orientation of the ATPase pore loops, with pre-sensor 1 loops arranged in a staircase configuration that follows the helical rise of the leading-strand template (Fig. 4d), as observed in the active CMG helicase (Extended Data Fig. 5c). Despite leading-strand DNA engagement by the pre-sensor 1 loops, our data do not indicate that SH actively translocate on DNA; instead, our ReconSil

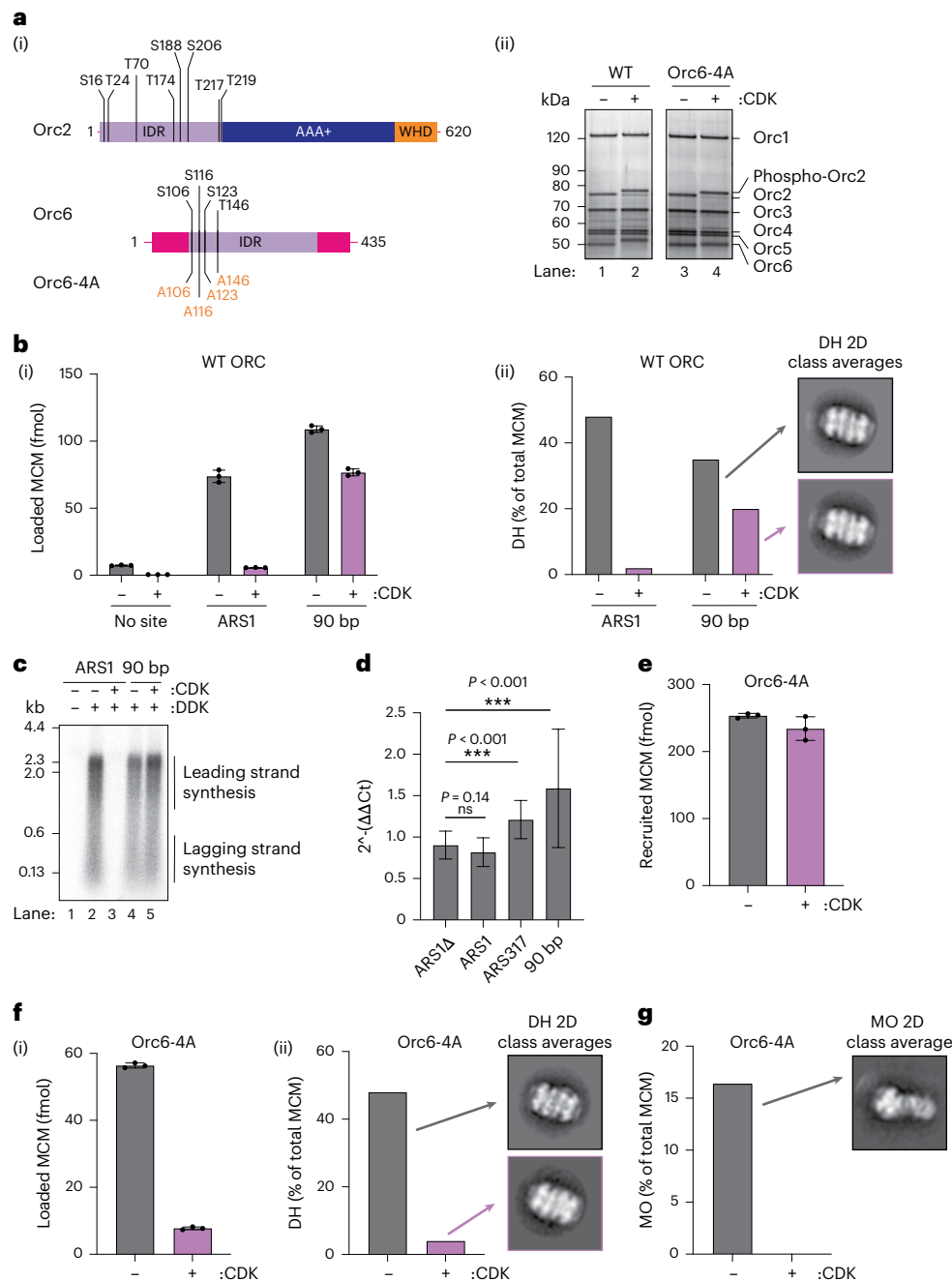


Fig. 3 | CDK phosphorylation of Orc2 inhibits the formation of MO.

a, (i) Potential CDK phosphorylation sites (consensus sequences $(S/T)PX^K/R$) in Orc2 and Orc6. (ii) An Orc6 mutant with four CDK target sites mutated to alanine (Orc6-4A) can be stably incorporated into the ORC complex but not phosphorylated. CDK phosphorylation of Orc2 in Orc6-4A-containing ORCs is comparable to WT. **b**, MCM loading on ARS1, but not 90 bp origins, is highly sensitive to CDK phosphorylation of ORC. The data in **b**(i) are plotted as the means of three technical replicates; error bars, s.d. Quantification of micrographs, total MCM and DH in negative-stain EM 2D classification data in **b**(ii): ARS1 – CDK (136, 3,531, 853); ARS1 + CDK (184, 4,748, 46); 90 bp – CDK (121, 3,392, 594); 90 bp + CDK (121, 4,587, 461). **c**, MCMs loaded onto 90 bp origins by phosphorylated ORC are replication competent. **d**, In yeast cells dependent on ORC phosphorylation to prevent re-replication, 90 bp spaced origins inserted

into the yeast genome re-replicate, causing an increase in copy number, as detected by qPCR. The data are plotted as means of three biological replicates, with each containing two technical replicates of triplicates; error bars, s.d.; $n = 18$. P values were obtained from two-tailed t -tests (ns, not significant). **e**, **f**, ORC phosphorylated on Orc2 by CDK (Orc6-4A mutant) efficiently recruits MCMs to ARS1 origins (**e**) but is inhibited in MCM loading (**f**). The data in **e** and **f**(i) are plotted as means of three technical replicates; error bars, s.d. Quantification of micrographs, total MCM and DH in negative-stain EM 2D classification data in **f**(ii): ARS1, Orc6-4A – CDK (128, 3,044, 724); ARS1, Orc6-4A + CDK (174, 5,971, 126). **g**, ORC phosphorylated on Orc2 by CDK (Orc6-4A mutant) fails to form MO. Quantification of micrographs, total MCM and MO in negative-stain EM 2D classification data: ARS1, Orc6-4A – CDK (159, 4,482, 735); ARS1, Orc6-4A + CDK (266, 7,115, not detected).

data (Fig. 4a) show SH randomly distributed across origins, having moved either in an N-terminal or C-terminal direction after loading. This result is consistent with single-molecule studies showing SH diffusion following loading by ORC^{31,32}.

Mechanism of MO-independent DH assembly

To examine the properties of the loaded SH, we assembled MCM with Orc2 Δ N on either a one-site template, in which only SH assembles, or a template containing two ORC binding sites separated by 90 bp,

Table 1 | Cryo-EM data collection, refinement and validation statistics

	MCM-SH (EMD-19187) (PDB 8RIG)	MCM-DH (EMD-19186) (PDB 8RIF)
Data collection and processing		
Magnification	×130,000	×130,000
Voltage (kV)	300	300
Electron exposure (e ⁻ Å ⁻²)	51.4	51.4
Defocus range (mm)	1.0–5.0	1.0–5.0
Pixel size (Å)	1.08	1.08
Symmetry imposed	C1	C2
Initial particle images (no.)	621,909	178,188
Final particle images (no.)	396,366	135,143
Map resolution (Å)		
RELION (PostProcess)	3.41	2.8
FSC threshold	0.143	0.143
Resolve cryo-EM	3.14	2.60
FSC _{ref} threshold	0.5	0.5
Map resolution range (Å)	2.2–4.0	2.2–3.8
Refinement		
Initial model used (PDB code)	8RIF	7P30
Map resolution (Å)	2.6	3.0
FSC _{ref} threshold	0.5	0.5
Map sharpening B factor (Å ²)	Resolve cryo-EM (27.3)	Resolve cryo-EM (0)
Model composition		
Non-hydrogen atoms	30,221	64,145
Protein residues	3,721	7,820
Nucleotides	38	106
Ligands (ATP, ADP, Mg ²⁺ , Zn ²⁺)	2 ATP, 4 ADP, 6 Mg ²⁺ , 5 Zn ²⁺	2 ATP, 6 ADP, 8 Mg ²⁺ , 10 Zn ²⁺
B factors (Å²)		
Protein	65.37	61.85
Nucleotide	20.00	102.70
Ligand	57.35	63.70
R.m.s. deviations		
Bond lengths (Å ²)	0.007	0.007
Bond angles (°)	1.117	1.232
Validation		
Molprobrity score	1.26	1.30
Clashscore	2.04	1.81
Poor rotamers (%)	0.97	0.98
Ramachandran plot		
Favored (%)	95.88	94.87
Allowed (%)	3.96	4.98
Disallowed (%)	0.16	0.16

in which DH efficiently forms. We then challenged the loaded MCM products with buffers containing different salt concentrations. As shown in Fig. 5a, MCM loaded on both templates was resistant to salt concentrations up to 250 mM NaCl; virtually all of the MCM was removed from the one-site templates at 500 and 1,000 mM NaCl,

whereas about 40% of the MCM remained on the 90 bp template after 500 and 1,000 mM NaCl washes. These experiments indicate that SH is stable up to ~250 mM NaCl but is efficiently removed at salt concentrations of 500 mM NaCl and above. The DH is stable up to 2 M NaCl³³, so the fraction of MCM removed by 500 mM NaCl from the 90 bp origin probably represents SH, with the MCM remaining at 500 and 1,000 mM NaCl being DH. This suggests that a substantial fraction of the MCM loaded even on this very efficient origin are SHs that have not matured into DHs. This is consistent with single-molecule experiments showing that SHs are readily detected during normal MCM loading reactions³¹.

To determine the off rate of SH under MCM loading conditions (low salt), MCM was loaded as above using Orc2ΔN on a single-site sequence, and excess protein was removed by low-salt wash (LSW). The amount of SH remaining on DNA was then assessed after incubation for the indicated times, followed by another LSW. Figure 5b shows that SHs were lost from DNA with a half-life of approximately 3.5 min. To compare this to the DH, we loaded MCM onto the 90 bp template and then washed free proteins and SHs off with high salt (1 M NaCl) before taking time points. As shown in Fig. 5b, DHs are stable for the entire duration of the experiment. Therefore, the SH is much less stable than the DH on DNA.

To show more directly that two independently loaded SHs can assemble into a DH, we generated a template with two high-affinity ORC sites separated by 300 bp and four lac operators between the sites (Fig. 5c). As a control, we also generated a template with a single ORC site and four lac operators. We pre-assembled SHs on these templates with Orc2ΔN for 20 min (Fig. 5d). As shown in Extended Data Fig. 6a, there is considerable MCM loaded on both templates at this point; however, this MCM is all removed by high-salt wash (HSW), indicating that there are no DHs. DH formation (high-salt-resistant MCM) was detected at significant levels only on the two ORC binding site templates and only after IPTG addition (Fig. 5e) in a time-dependent manner. This strongly supports the idea that two SHs can generate a DH after interaction. To exclude the possibility that loading occurs via MO, we repeated the experiment in Fig. 5e except we removed all free MCM–Cdt1 and Cdc6 by washing the beads before adding IPTG (Extended Data Fig. 6b). Extended Data Fig. 6c shows that these washes effectively remove all Cdt1 from reactions before IPTG addition in reactions containing ATP, but not ATPγS, where Cdt1 remains as part of the OCCM complex. Extended Data Fig. 6d shows the amount of MCM loaded onto DNA in ATP (one-site and two-site) after salt washes and shows that all of this MCM is removed by HSW, consistent with the complete lack of DH. Extended Data Fig. 6e shows high-salt-resistant MCM loading after IPTG addition, confirming that DH assembly occurs entirely from SHs that were loaded before IPTG addition without a requirement for Cdc6, Cdt1 or free MCM. The overall amount of DH assembled in this experiment (~12 fmol) is lower than the amount formed in Fig. 5e (~45 fmol). We believe that this is a consequence of the loss of SHs during washing before IPTG addition. The presence of 150 fmol of SH after washes at the point of IPTG addition (Extended Data Fig. 6d), distributed randomly on 300 fmol ORC binding site, predicts that only 25% of DNA molecules (37.5 fmol) at this point have two SHs, a prerequisite for DH assembly. Furthermore, because the two ORC sites in this template are 300 bp apart, we would expect a further reduction in loading efficiency of around 50% (see below). Consequently, the maximum loading we might expect under these conditions should be less than 20 fmol. Taken together, these experiments show that DH can assemble from loaded SHs in the absence of Cdc6, Cdt1 and free MCM.

The efficiency of DH assembly decreases as the two ORC sites are moved farther than ~90 bp apart. We reasoned that the farther apart two SHs are loaded, the higher the probability that one or the other will fall off before meeting. To model this process, we used the observed one-dimensional diffusion constant for the DH³⁴, together with the off rate determined in Fig. 5b (Extended Data Fig. 7), and, as shown in Fig. 5f, the predicted loading efficiencies are remarkably close to those seen in the experimental data. Diffusion could occur with

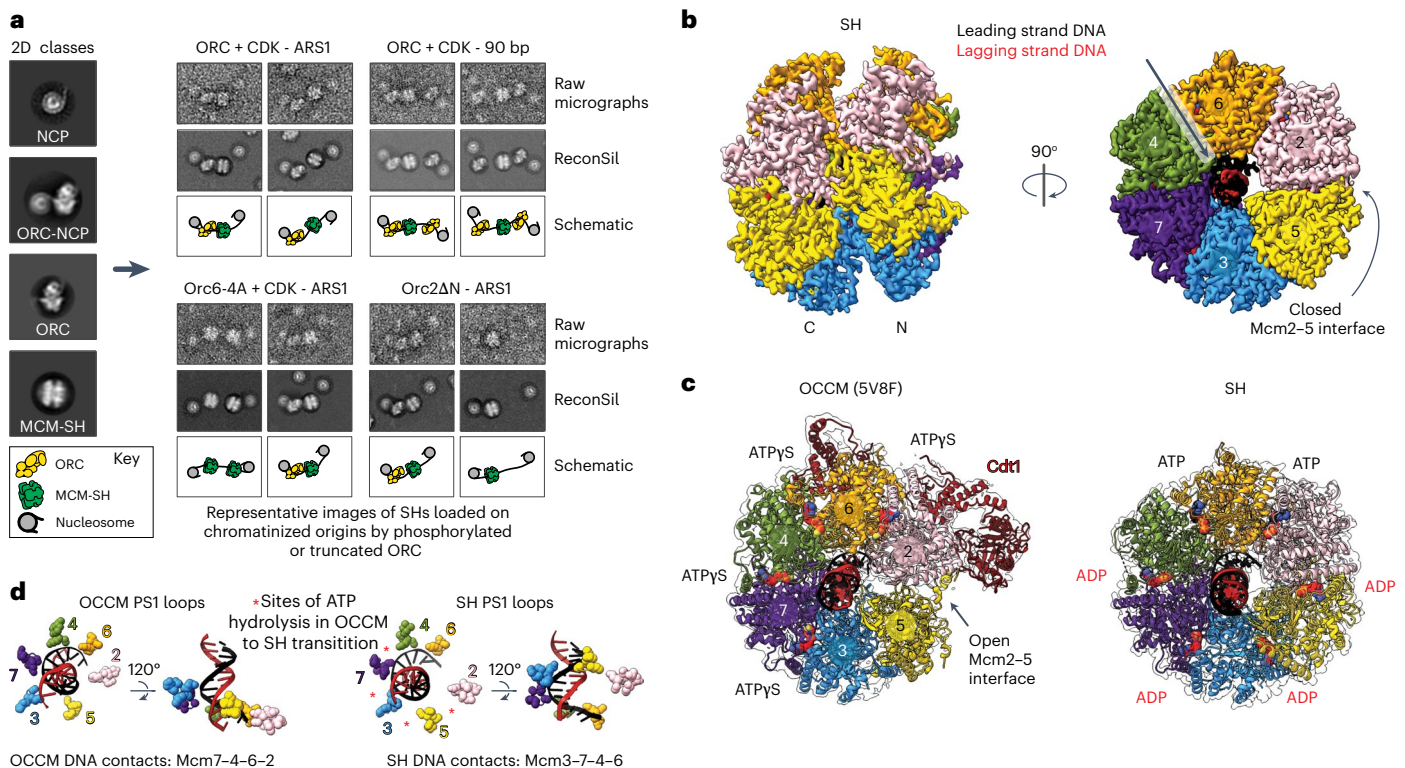


Fig. 4 | Structure of the MCM-SH. **a**, Negative-stain EM ReconSil of MCM loading reactions performed with phosphorylated or truncated Orc2. Left, conventional EM 2D class averages. Right, representative images of chromatized origins bound by single MCM helicases with or without DNA-bound ORCs and flanked by nucleosomes, shown as raw micrographs (top rows), after ReconSil (middle rows) or as schematics (bottom rows). **b**, Cryo-EM structure of a DNA-bound SH.

c, Cryo-EM structures and atomic models for OCCM (PDB 5V8F (ref. 46)) and a SH. The EM density map displayed for the SH has been density-modified using EMReady⁴⁵. **d**, ATP hydrolysis in the Mcm4-7, Mcm7-3, Mcm3-5 and Mcm5-2 ATPase sites during SH loading is associated with a reconfiguration of the MCM pre-sensor 1 (PS1) loops into a staircase configuration that engages the leading-strand template DNA backbone.

rotation following the path of the DNA helix, or by diffusion without rotation. For several reasons, we favor the idea that movement occurs coupled with rotation tracking the DNA helix. First, the structure of the SH shows a single mode of DNA engagement within the MCM central channel, with individual nucleotides clearly resolved (Extended Data Fig. 5d). Despite the large number of particles (~400,000), further 3D classification failed to detect SHs with an alternate DNA engagement, suggesting that the DNA register remains the same in all imaged SHs, regardless of their relative position on the origin DNA. If SHs diffused without rotation, they would be unlikely to have a highly preferred mode of DNA engagement. Second, without rotation, two SHs would meet in different registers depending on how far apart the loading sites were. One might expect to see evidence of this in loading efficiency; however, Fig. 5g shows that loading efficiency is very similar at every distance from 70–93 bp. Rotation along the DNA helix ensures that the two SHs always meet with the same register; using the first steric clash between hexamers as the end point of rotational diffusion along B-form DNA, this register is very close to the register seen in the DH (Supplementary Video 1). Taken together, we propose that DH assembly occurs by random rotational diffusion and meeting of two SH along the DNA, followed by a presently uncharacterized ‘locking’ of the two into a stable DH.

Discussion

Our results, summarized in Fig. 5h, indicate that MCM can be loaded by at least three distinct pathways in budding yeast. In each pathway, the unifying mechanism is the loading of two SHs with inverted orientations. DH assembly can be coordinated by the MO, which facilitates ORC recruitment to a weak DNA site. Alternatively, DH assembly can

be done in the absence of the MO, in which case two independently loaded SHs translocate by rotation along the helical axis until meeting to form a stable DH. The loading of the SH defines a precise register of DNA engagement that ensures two loaded SHs with inverted orientations will always meet in the same subunit register, regardless of the distance between their loading sites. Our data (Fig. 2b) show that DH formation is at least as efficient without MO as with MO, indicating that the SH to DH ‘locking’ mechanism is intrinsic to two correctly oriented and DNA-engaged SHs and is independent of the MO. We cannot rule out the possibility that some SH movement is directional and coupled to ATP hydrolysis; however, for two reasons, we favor a mechanism whereby DH formation occurs upon collision of two SHs that randomly slide along the helical axis of DNA. First, because of the wide distribution in distances between ORC binding sites at origins, it is sometimes necessary for SH to move in a C-terminal direction (for example, at ARS1) and sometimes in an N-terminal direction. A priori, this is best accommodated by random motion. Second, our ReconSil images show SH that have been imaged after movement in either direction from their loading site (Fig. 4a). If SH moved directionally, we would expect to see them accumulate with their N-termini adjacent to nucleosomes (or a downstream ORC). Instead, we find SH at a range of positions, including instances in which the SH has moved in a C-terminal direction to occupy the site previously occupied by ORC. This result is consistent with previous single-molecule studies showing MCM single hexamer diffusion after loading^{31,32}.

SHs are considerably less stable on DNA than DHs. We suggest that this is because the Mcm2-5 interaction is intrinsically weak, providing a gate for DNA to exit the central channel. This could explain recent FRET experiments showing that the Mcm2-5 gate is not stably

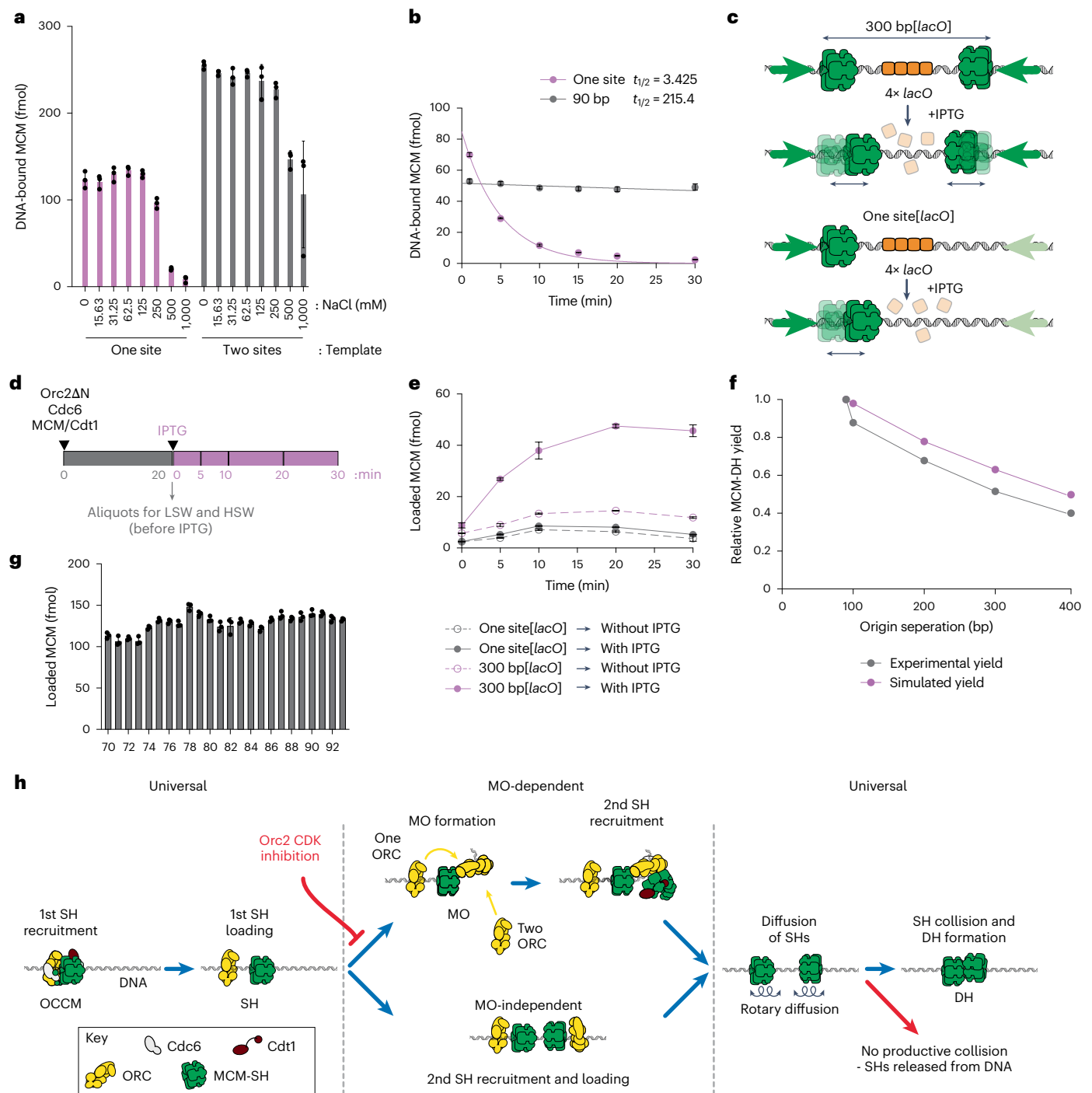


Fig. 5 | Mechanism of MO-independent DH formation. **a, b**, SHs have a lower salt stability (**a**) and a shorter half-life ($t_{1/2}$) (**b**) on DNA than DHs. The data in **a** and **b** are plotted as means of three technical replicates; error bars, s.d. **c, d**, Schematics illustrating origins (**c**) and assay (**d**) used for characterizing MO-independent DH formation via collision of two independently loaded SHs. **e**, Aliquots were taken at different time points for HSW. The amount of MCM was significantly increased on the 300 bp[*lacO*] template after HSW, indicating that two independently loaded SHs formed a DH. In the presence of IPTG, approximately 3.8-fold more MCM was detected on the 300 bp[*lacO*] at 30 min compared to the reaction without IPTG. The data are plotted as means of three technical replicates; error bars, s.d. **f**, Efficiency of DH formation decreases with

increase in separation between ORC binding sites and can be modeled as the meeting probability of two diffusing SHs loaded at ORC binding sites at a given separation in the experimental time (20 min). The experimental yield data were obtained from the mean of three datasets. **g**, MCM loading is insensitive to the separation distance between two ORC binding sites (between 70 and 93 bp) and relative orientation of recruited ORCs with respect to each other along the DNA helix. The data are plotted as means of three technical replicates; error bars, s.d. **h**, Proposed model for MCM loading via MO-dependent and independent pathways. Both pathways converge on a 'universal' mechanism that requires loading of two SHs that must collide in a head-to-head orientation to form a DH.

closed after first hexamer loading by ORC after Orc2 phosphorylation¹³. Although this was interpreted as meaning phosphorylation prevented ring closure, our results indicate that gate closure occurs, but the SH ring is unstable. The Mcm2–5 gates are not aligned in the DH but are located approximately 180° apart; therefore, even if both gates open at the same time, the DH would remain topologically bound around DNA³⁵, which may prevent dissociation of the DH. Alternatively, contacts between the hexamers may stabilize the Mcm2–5 gate in the DH, preventing opening¹³. Our experiments have not addressed the role of Orc6 phosphorylation, which will be interesting to explore.

Previous work in yeast has shown that a substantial fraction of MCM is released from G1 chromatin with a moderate salt concentration (350 mM NaCl)³⁶, suggesting the presence of SH on chromatin. From yeast to humans, the total amount of MCM bound to chromatin far exceeds the number of active replication origins. This ‘MCM paradox’ has been explained, at least in part, by the existence of dormant origins that are activated under stress conditions^{37–40}; our results suggest that in addition, some of the excess MCM may be in the form of SH, which cannot support replication (for example, Figs. 2d and 3c). SHs are relatively short-lived, but there may also be active mechanisms to remove them from chromatin. Further work is required to assess what fraction of chromatin-bound MCM is SH.

Synthetic origins comprising two high-affinity ORC binding sites load MCM even more efficiently than ARS1 (for example, Fig. 2b) and function as autonomously replicating sequences *in vivo*⁵. Moreover, replication origins in *Archaea*, the progenitor replication system of eukaryotes, generally comprise multiple, high-affinity ORC sites in opposite orientations and at distances similar to our synthetic origins. However, yeast origins generally have a single high-affinity site flanked by low-affinity sites, indicating that MO-dependent DH assembly is likely to be the predominant mode of MCM loading *in vivo*. Our work suggests an explanation for this: origins with two high-affinity sites cannot be inhibited by CDK phosphorylation of Orc2 (Fig. 3c,d). We propose that this arrangement has been selected against during evolution: co-evolution of sequence-specific DNA binding by ORC^{41,42} and CDK regulation of ORC function has resulted in the asymmetry in modern yeast replication origins. Whether MO-dependent DH assembly *in vivo* proceeds via one or two ORC pathways is unclear, given that we do not know the concentration of free ORC in cells and currently lack a mutant that can distinguish these pathways. The ability of Orc2ΔN or CDK-phosphorylated Orc2 to load low levels of DHs at endogenous origins like ARS1 may help explain why three other CDK targets (Orc6, Cdc6 and Mcm3) are required to completely block MCM loading outside of G1 phase in yeast.

Human Orc2 also contains a long N-terminal IDR⁴³ but has no detectable sequence similarity to the yeast IDR. Recent work has shown that human ORC can load MCM through an MO-independent mechanism that does not require Orc6 and a mechanism that involves an MO-like intermediate. This mechanism does not appear to involve the Orc2 IDR, consistent with the hypothesis that CDK regulation of the MO by the Orc2 IDR co-evolved with the structure of yeast origins. Orc2 from multicellular plants entirely lacks an N-terminal IDR; therefore, plants are unlikely to use the same MO-dependent mechanism. Whether plants and metazoans use a mechanism related to the two ORC MO-independent mechanism or some other, novel mechanism requires further work. Finally, the recent sequencing of several metamonad genomes has shown that although all six MCM genes are present, organisms in the genus *Carpodomonas* lack all ORC subunits, Cdc6 and Cdt1 (ref. 44), indicating additional MCM loading mechanisms remain to be discovered.

Online content

Any methods, additional references, Nature Portfolio reporting summaries, source data, extended data, supplementary information, acknowledgements, peer review information; details of author contributions

and competing interests; and statements of data and code availability are available at <https://doi.org/10.1038/s41594-025-01591-9>.

References

- Lin, Y. C. & Prasanth, S. G. Replication initiation: implications in genome integrity. *DNA Repair (Amst.)* **103**, 103131 (2021).
- Hu, Y. & Stillman, B. Origins of DNA replication in eukaryotes. *Mol. Cell* **83**, 352–372 (2023).
- Costa, A. & Diffley, J. F. X. The initiation of eukaryotic DNA replication. *Annu. Rev. Biochem.* **91**, 107–131 (2022).
- Palzkil, T. G. & Newlon, C. S. A yeast replication origin consists of multiple copies of a small conserved sequence. *Cell* **53**, 441–450 (1988).
- Coster, G. & Diffley, J. F. X. Bidirectional eukaryotic DNA replication is established by quasi-symmetrical helicase loading. *Science* **357**, 314–318 (2017).
- Bell, S. P. & Stillman, B. ATP-dependent recognition of eukaryotic origins of DNA replication by a multiprotein complex. *Nature* **357**, 128–134 (1992).
- Rao, H. & Stillman, B. The origin recognition complex interacts with a bipartite DNA binding site within yeast replicators. *Proc. Natl Acad. Sci. USA* **92**, 2224–2228 (1995).
- Rowley, A., Cocker, J. H., Harwood, J. & Diffley, J. F. X. Initiation complex assembly at budding yeast replication origins begins with the recognition of a bipartite sequence by limiting amounts of the initiator, ORC. *EMBO J.* **14**, 2631–2641 (1995).
- Ticau, S. et al. Mechanism and timing of Mcm2–7 ring closure during DNA replication origin licensing. *Nat. Struct. Mol. Biol.* **24**, 309–315 (2017).
- Ticau, S., Friedman, L. J., Ivica, N. A., Gelles, J. & Bell, S. P. Single-molecule studies of origin licensing reveal mechanisms ensuring bidirectional helicase loading. *Cell* **161**, 513–525 (2015).
- Miller, T. C. R., Locke, J., Greiwe, J. F., Diffley, J. F. X. & Costa, A. Mechanism of head-to-head MCM double-hexamers formation revealed by cryo-EM. *Nature* **575**, 704–710 (2019).
- Gupta, S., Friedman, L. J., Gelles, J. & Bell, S. P. A helicase-tethered ORC flip enables bidirectional helicase loading. *eLife* <https://doi.org/10.7554/eLife.74282> (2021).
- Amasino, A. L., Gupta, S., Friedman, L. J., Gelles, J. & Bell, S. P. Regulation of replication origin licensing by ORC phosphorylation reveals a two-step mechanism for Mcm2–7 ring closing. *Proc. Natl Acad. Sci. USA* **120**, e2221484120 (2023).
- Jumper, J. et al. Highly accurate protein structure prediction with AlphaFold. *Nature* **596**, 583–589 (2021).
- Li, N. et al. Structure of the origin recognition complex bound to DNA replication origin. *Nature* **559**, 217–222 (2018).
- Evans, R. et al. Protein complex prediction with AlphaFold-Multimer. Preprint at <https://doi.org/10.1101/2021.10.04.463034> (2022).
- Perkins, G., Drury, L. S. & Diffley, J. F. X. Separate SCF^{CDC4} recognition elements target Cdc6 for proteolysis in S phase and mitosis. *EMBO J.* **20**, 4836–4845 (2001).
- Drury, L. S., Perkins, G. & Diffley, J. F. X. The cyclin-dependent kinase Cdc28p regulates distinct modes of Cdc6p proteolysis during the budding yeast cell cycle. *Curr. Biol.* **10**, 231–240 (2000).
- Drury, L. S., Perkins, G. & Diffley, J. F. X. The Cdc4/34/53 pathway targets Cdc6p for proteolysis in budding yeast. *EMBO J.* **16**, 5966–5976 (1997).
- Elsasser, S., Chi, Y., Yang, P. & Campbell, J. L. Phosphorylation controls timing of Cdc6p destruction: a biochemical analysis. *Mol. Biol. Cell* **10**, 3263–3277 (1999).
- Moses, A. M., Liku, M. E., Li, J. J. & Durbin, R. Regulatory evolution in proteins by turnover and lineage-specific changes of cyclin-dependent kinase consensus sites. *Proc. Natl Acad. Sci. USA* **104**, 17713–17718 (2007).

22. Liku, M. E., Nguyen, V. Q., Rosales, A. W., Irie, K. & Li, J. J. CDK phosphorylation of a novel NLS–NES module distributed between two subunits of the Mcm2–7 complex prevents chromosomal rereplication. *Mol. Biol. Cell* **16**, 5026–5039 (2005).
23. Nguyen, V. Q., Co, C., Irie, K. & Li, J. J. Clb/Cdc28 kinases promote nuclear export of the replication initiator proteins Mcm2–7. *Curr. Biol.* **10**, 195–205 (2000).
24. Labib, K., Diffley, J. F. X. & Kearsley, S. E. G1-phase and B-type cyclins exclude the DNA-replication factor Mcm4 from the nucleus. *Nat. Cell Biol.* **1**, 415–422 (1999).
25. Tanaka, S. & Diffley, J. F. X. Interdependent nuclear accumulation of budding yeast Cdt1 and Mcm2–7 during G1 phase. *Nat. Cell Biol.* **4**, 198–207 (2002).
26. Yeeles, J. T., Deegan, T. D., Janska, A., Early, A. & Diffley, J. F. X. Regulated eukaryotic DNA replication origin firing with purified proteins. *Nature* **519**, 431–435 (2015).
27. Frigola, J., Remus, D., Mehanna, A. & Diffley, J. F. X. ATPase-dependent quality control of DNA replication origin licensing. *Nature* **495**, 339–343 (2013).
28. Chen, S. & Bell, S. P. CDK prevents Mcm2–7 helicase loading by inhibiting Cdt1 interaction with Orc6. *Genes Dev.* **25**, 363–372 (2011).
29. Nguyen, V. Q., Co, C. & Li, J. J. Cyclin-dependent kinases prevent DNA re-replication through multiple mechanisms. *Nature* **411**, 1068–1073 (2001).
30. Richardson, C. D. & Li, J. J. Regulatory mechanisms that prevent re-initiation of DNA replication can be locally modulated at origins by nearby sequence elements. *PLoS Genet.* **10**, e1004358 (2014).
31. Sanchez, H. et al. DNA replication origins retain mobile licensing proteins. *Nat. Commun.* **12**, 1908 (2021).
32. Zhang, A., Friedman, L. J., Gelles, J. & Bell, S. P. Changing protein–DNA interactions promote ORC binding-site exchange during replication origin licensing. *Proc. Natl Acad. Sci. USA* **120**, e2305556120 (2023).
33. Frigola, J. et al. Cdt1 stabilizes an open MCM ring for helicase loading. *Nat. Commun.* **8**, 15720 (2017).
34. Sanchez, H. et al. A chromatinized origin reduces the mobility of ORC and MCM through interactions and spatial constraint. *Nat. Commun.* **14**, 6735 (2023).
35. Hizume, K., Kominami, H., Kobayashi, K., Yamada, H. & Araki, H. Flexible DNA path in the MCM double hexamer loaded on DNA. *Biochemistry* **56**, 2435–2445 (2017).
36. Donovan, S., Harwood, J., Drury, L. S. & Diffley, J. F. X. Cdc6p-dependent loading of Mcm proteins onto pre-replicative chromatin in budding yeast. *Proc. Natl Acad. Sci. USA* **94**, 5611–5616 (1997).
37. Santocanale, C., Sharma, K. & Diffley, J. F. X. Activation of dormant origins of DNA replication in budding yeast. *Genes Dev.* **13**, 2360–2364 (1999).
38. Vujcic, M., Miller, C. A. & Kowalski, D. Activation of silent replication origins at autonomously replicating sequence elements near the HML locus in budding yeast. *Mol. Cell. Biol.* **19**, 6098–6109 (1999).
39. Ibarra, A., Schwob, E. & Mendez, J. Excess MCM proteins protect human cells from replicative stress by licensing backup origins of replication. *Proc. Natl Acad. Sci. USA* **105**, 8956–8961 (2008).
40. Woodward, A. M. et al. Excess Mcm2–7 license dormant origins of replication that can be used under conditions of replicative stress. *J. Cell Biol.* **173**, 673–683 (2006).
41. Hu, Y. et al. Evolution of DNA replication origin specification and gene silencing mechanisms. *Nat. Commun.* **11**, 5175 (2020).
42. Lee, C. S. K. et al. Humanizing the yeast origin recognition complex. *Nat. Commun.* **12**, 33 (2021).
43. Parker, M. W. et al. A new class of disordered elements controls DNA replication through initiator self-assembly. *eLife* <https://doi.org/10.7554/eLife.48562> (2019).
44. Salas-Leiva, D. E. et al. Genomic analysis finds no evidence of canonical eukaryotic DNA processing complexes in a free-living protist. *Nat. Commun.* **12**, 6003 (2021).
45. He, J., Li, T. & Huang, S. Y. Improvement of cryo-EM maps by simultaneous local and non-local deep learning. *Nat. Commun.* **14**, 3217 (2023).
46. Yuan, Z. et al. Structural basis of Mcm2–7 replicative helicase loading by ORC–Cdc6 and Cdt1. *Nat. Struct. Mol. Biol.* **24**, 316–324 (2017).

Publisher's note Springer Nature remains neutral with regard to jurisdictional claims in published maps and institutional affiliations.

Open Access This article is licensed under a Creative Commons Attribution 4.0 International License, which permits use, sharing, adaptation, distribution and reproduction in any medium or format, as long as you give appropriate credit to the original author(s) and the source, provide a link to the Creative Commons licence, and indicate if changes were made. The images or other third party material in this article are included in the article's Creative Commons licence, unless indicated otherwise in a credit line to the material. If material is not included in the article's Creative Commons licence and your intended use is not permitted by statutory regulation or exceeds the permitted use, you will need to obtain permission directly from the copyright holder. To view a copy of this licence, visit <http://creativecommons.org/licenses/by/4.0/>.

© The Author(s) 2025

Methods

Strains

All primers, plasmids and strains used for strain construction are listed in Supplementary Tables 1, 2 and 3, respectively. The YJL3239 strain was a gift from J. Li²⁹. The ARS317, ARS1, ARS1Δ and synthetic 90 bp origins were inserted in ARS419 using a previously described method³⁰ with some modifications. The endogenous ARS317 was deleted and replaced with kanMX6 from pFA6a-3HA-kanMX6 with amplification using CTL61 and CTL62 (yCTL5). URA3 was replaced with hphNT1 from pFA6a-hphNT1 with amplification using CTL98 and CTL99 (yCTL18). URA3 was amplified using pRS306 with primers CTL86 and CTL87 and additionally inserted in ARS419 at position 567 kb in Chromosome IV (yCTL19). The ARS317, ARS1, ARS1Δ and synthetic 90 bp origins were amplified from plasmid ARS317-Abf1(pCTL69), ARS1-Abf1 (pCTL68), ARS1Δ (pGC404 in ref. 5) and 90bp-Abf1 (pCTL67), respectively, using CTL160 and CTL161 and counter-selected with 5-FOA (Melford), resulting in strains yCTL30, yCTL29, yCTL28 and yCTL33. A total of 1 mg ml⁻¹ of 5-FOA was added to minimal media containing 1× YNB, 2% glucose, 1× complete supplement mixture and 80 μg ml⁻¹ uracil. The ARS317-RIP sequence was identified according to the L4-L12 region in a previous work³⁰.

The sequence for the Orc6 phosphorylation mutant Orc6-4A was obtained from Invitrogen GeneArt Synthesis (Thermo Fisher Scientific). This sequence was then used to replace the WT Orc6 in the plasmid pJF18, as in a previous publication²⁷, to create strain yCTL6 (Orc6-4A). Endogenous Orc6 was Flag-tagged to allow removal of the endogenous WT protein.

Amino acids 2–235 in Orc2 were deleted in the Orc2 N-terminal truncation mutant (Orc2ΔN). This mutant was introduced into pJF19, as in a previous publication²⁷, to replace the WT Orc2. The WT Orc2 was Flag-tagged so that the endogenous protein could be removed. The resulting strain was named yCTL17.

Protein expression and purification

In this study, ORC, Cdc6, Luc-MCM/Cdt1, CDK and Sic1 were expressed and purified according to previously described methods^{5,26,27}. The Orc2ΔN mutant was purified identically to WT ORC, but with the additional step of using Flag beads after CBP pulldown to remove endogenous WT proteins. The same was done for the Orc6 phosphorylation mutants.

ORC binding assay

ORC binding assays were performed as previously described⁵. In brief, 0.25 pmol DNA of 0.6 kb PCR substrates with a single biotin (GC117 and GC298) were coupled with 5 μl of Dynabeads M-280 streptavidin (Invitrogen, 11205D) in 10 μl of binding buffer (5 mM Tris-HCl pH 8.0, 0.5 mM EDTA, 1 M NaCl), for 30 min at 30 °C with mixing at 1,250 rpm in a 1.5 ml microcentrifuge tube. Beads were washed twice and resuspended in buffer containing 10 mM HEPES-KOH pH 7.6 and 1 mM EDTA. The bead-bound DNA substrate was then incubated with 20 nM ORC in 40 μl loading buffer (25 mM HEPES-KOH pH 7.6, 100 mM NaOAc, 10 mM MgOAc, 0.02% NP-40, 5% glycerol, 1 mM dithiothreitol (DTT), 5 mM ATP, 80 mM KCl). The reaction was incubated for 15 min at 30 °C with mixing at 1,600 rpm on a 96-well plate. Reactions were then washed twice with LSW additionally containing 80 mM NaCl (45 mM HEPES-KOH pH 7.6, 5 mM MgOAc, 300 mM NaOAc, 0.02% NP-40, 10% glycerol, 2 mM CaCl₂, 80 mM NaCl) for 2 min, 30 °C at 1,600 rpm. A total of 150 mM of NaCl was used in the washing step in Extended Data Fig. 2d. The washed beads were then washed once with LSW again before resuspending in 15 μl LSW with 600 units of micrococcal nuclease (MNase; NEB, M0247S) and incubated for 2 min, 30 °C at 1,600 rpm. The supernatant from the two reactions was collected and separated by Criterion XT Tris Acetate 3–8% (Bio-Rad) SDS-PAGE and visualized by silver staining.

MCM loading

The MCM loading assay was performed as previously described⁵. Biotinylated DNA substrate (0.15 pmol) was attached to magnetic beads and

then incubated with 12 nM ORC, 20 nM Cdc6, 80 nM Luc-MCM/Cdt1 in 40 μl loading buffer for 20 min at 30 °C with mixing at 1,600 rpm. Beads were washed twice with HSW (45 mM HEPES-KOH pH 7.6, 5 mM MgOAc, 0.02% NP-40, 10% glycerol, 1 M NaCl) for 2 min and twice with LSW (45 mM HEPES-KOH pH 7.6, 5 mM MgOAc, 300 mM NaOAc, 0.02% NP-40, 10% glycerol, 2 mM CaCl₂) for 20 s. Proteins were released by 30 μl of LSW with MNase treatment for 2 min and transferred to white, flat-bottom, half-area 96-well plates (Corning, 3642). Nano-Glo Luciferase assay substrate (Promega N1120) was diluted 1:50, and 30 μl of diluted substrate was added to the sample. A standard curve was also prepared with a 2.5-fold dilution of Luc-MCM (ranging from 0.027–256.33 fmol). The luminescence was measured on a PHERAstar plate reader using 'LUM Plus' optic module (BMG Labtech) with the read time of 1 s per well at 12.1 mm focal height. The background (LSW only) was subtracted, and the amount of Luc-MCM was calculated using a linear regression of the standard curve of Luc-MCM. All experiments were done in triplicate. In the staged reaction depicted in Fig. 2g, ORC at various concentrations was preincubated with DNA beads for 15 min at 30 °C with mixing at 1,600 rpm. The reaction was washed twice with LSW + 150 mM NaCl buffer described above. Then, 40 nM Cdc6 and 80 nM MCM-Cdt1 were added to the reaction and incubated for another 5 min.

In the inducible roadblock assay, beads were resuspended in 20 μl binding buffer (25 mM HEPES-KOH pH 7.6, 100 mM NaOAc, 10 mM MgOAc, 0.02% NP-40, 5% glycerol, 5 mM DTT, 80 mM KCl). Then, 2.4 pmol of Lacl (a gift from G. Cameron and H. Yardimci⁴⁷) was added and incubated for 30 min at 30 °C with mixing at 1,250 rpm. The beads were washed twice and resuspended in 5 μl of binding buffer. This mixture was subsequently added to the MCM loading reaction and incubated for 20 min. Following this, 10 mM of IPTG and a 50× molar excess of competitor DNA containing one ORC binding site (EACS.B1F and EACS.B1R) were added. The reaction was aliquoted at the indicated time points for HSW, followed by LSW, as described above.

The conditions depicted in Extended Data Fig. 7 were the same as in Fig. 5e, except 9.6 pmol of Lacl was used. After incubation with MCM for 20 min (before the addition of IPTG), beads were washed twice in 45 mM HEPES-KOH pH 7.6, 5 mM MgOAc, 200 mM NaOAc, 0.02% NP-40, 10% glycerol and 2 mM CaCl₂. For the western blot, the samples were run on a 3–8% polyacrylamide gel (Invitrogen), immunoblotted and detected using Pierce ECL (Thermo Scientific) reagents. Polyclonal antibody JDI70 was used to detect Cdt1 (ref. 48) at a dilution of 1:2,500. Polyclonal antibody against Mcm6 (E78) was raised against a peptide containing Mcm6 residues 1,005–1,017 and was used at a dilution of 1:1,000 in this assay.

MCM recruitment

MCM recruitment assay was performed identically to the MCM loading assay, with the exception that 5 mM ATP was replaced with 5 mM ATPγS. After the incubation, the beads were washed twice with an ice-cold LSW for 20 s.

All experiments in the luciferase assays were done in triplicate, and the data are plotted as mean ± s.d.

CDK phosphorylation of ORC

For CDK-phosphorylated ORC, 12 nM of ORC was incubated with 12 nM CDK for 10 min at 30 °C in loading buffer containing 0.5 mM ATP. To stop the reaction, 60 nM Sic1 was added and incubated for an additional 5 min at 30 °C. For non-phosphorylated ORC, 12 nM ORC was first incubated with 60 nM Sic1 for 5 min at 30 °C and then with 12 nM CDK for 10 min at 30 °C. The subsequent loading assay was done as described above. For Fig. 3a, proteins were separated by Criterion XT Tris Acetate 3–8% (Bio-Rad) SDS-PAGE and visualized by silver staining.

Salt sensitivity assay

The salt sensitivity assay was performed identically to the MCM loading assay. After 20 min incubation, the samples were washed twice with

cold LSW containing the indicated NaCl concentration (as shown in Fig. 5a) for 30 s, followed by two washes with cold LSW.

Retention assay

The retention assay was performed identically to the MCM loading assay. After 20 min of incubation, the beads were washed with HSW (for 90 bp origin only) and then cold loading buffer (for both the one-site and 90 bp origins) for 40 s at 30 °C with mixing at 1,600 rpm. Then, 50× molar excess of competitor DNA in loading buffer (preheated at 30 °C) was added, and the mixture was aliquoted for an additional wash with HSW (for 90 bp origin only), followed by cold LSW (for both the one-site and 90 bp origins) at the indicated times.

Replication assay

The replication assays were performed according to a previously described protocol²⁶ with modifications. In brief, 48 nM ORC/Orc2ΔN /phosphorylated ORC (pre-phosphorylation of Orc6-4A with 50 nM CDK for 10 min at 30 °C), 80 nM Cdc6, 320 nM MCM-Cdt1 and 16 nM DNA were incubated for 20 min at 30 °C, 1,250 rpm in reaction buffer containing 25 mM HEPES-KOH pH 7.6, 10 mM MgOAc, 2 mM DTT, 0.02% NP-40, 100 mM KCl, 5 mM ATP and 80 mM KCl. Next, 50 nM DDK and 50 nM CDK were added with further incubation for 10 min. The mixture was diluted 4× in replication mix as follows: 20 nM Cdc45, 15 nM Dpb11, 20 nM Pol ε, 10 nM GINS, 50 nM RPA, 5 nM TopoI, 30 nM CDK, 50 nM Pol α, 13 nM Sld3/7, 10 nM Mcm10, 3 nM Sld2, 33 μM ³²P-dCTP, 200 μM NTPs and 80 μM dNTPs for 30 min, 30 °C, 1,250 rpm. The reactions were then stopped by adding 50 mM EDTA (final concentration) and filtered through an Illustra Microspin G-50 column. The replication products were resuspended in loading buffer and separated through 0.8% alkaline agarose gels in 30 mM NaOH and 2 mM EDTA for 16 h at 25 V. Gels were fixed with 5% cold trichloroacetic acid and then dried onto chromatography paper (Whatman) and autoradiographed with Amersham Hyperfilm-MP (GE Healthcare). Gel images were scanned using a Typhoon phosphorimager (GE Healthcare) and were quantified using ImageJ.

Electrophoretic mobility shift assays

Double-stranded DNA probes for electrophoretic mobility shift assays (EMSA) were generated by PCR using primers (50 bp up 209 and 50 bp down 209) to give 265 bp probes. A full list of primers and plasmids used for DNA templates is given in Supplementary Tables 1 and 2.

A total of 62.5 ng gel-purified PCR product (Nucleosin Gel and PCR clean-up, 740609.250 Macherey Nagel) was 5'-end-labeled in a final volume of 10 μl using 0.6 μl T4 PNK (10 U μl⁻¹; New England Biolabs, M0201) with 2 μl [γ -³²P]ATP (3,000 Ci mmol⁻¹; SRP-301 Hartmann). After 1 h on ice, 40 μl 10 mM HEPES-KOH pH 7.6, 1 mM EDTA was added, and unincorporated nucleotides were removed by passing through 2× microspin G-50 columns (Cytiva, GE27-5330-02), pre-spun for 1 min at 735g, followed by elution for 2 min at 735g.

For each EMSA reaction, 12 fmol of DNA probe was used (assuming 80% elution losses per column). Reaction components were added on ice to give a final concentration of 25 mM HEPES-KOH pH 7.6, 10 mM MgOAc, 100 mM NaOAc, 0.02% NP-40, 5 mM DTT, 80 mM KCl, 5% glycerol, 2 μg ml⁻¹ poly dl-dC and 5 mM ATP. Lastly, 100 fmol of purified ORC was added as required, and the reactions were incubated for 30 min at 30 °C in a thermomixer at 800 rpm. After 30 min, the samples were placed on ice, and 2 μl loading dye (Purple gel loading dye, no SDS; New England Biolabs, B7025) was added before loading 12 μl onto a 1.5% 15 × 15 cm 100 ml 0.5× TB agarose gel. The gel was run for 1 h at 200 V (4 °C) before fixation for 30 min in 5% TCA and drying on a vacuum gel dryer at 55 °C for 1 h (Hoefer, GD2000). After overnight exposure to a storage phosphor screen (GE Healthcare, BAS-IP MS 2025 E), the signal was detected using a Typhoon FLA7000 phosphorimager.

Induction of re-replication

Cells were grown overnight in medium lacking methionine and containing 2% raffinose (1× YNB, 1× CSM-Met; Formedium, DCS011). At a density of about 1 × 10⁷ cells per ml, 50 ng ml⁻¹ alpha factor was added to arrest the cell growth for 3 h. Cells were spun down and switched to YPRaff medium with alpha factor for 1 h. Cells were washed twice with YPRaff media (1× with YPRaff and 1× with YPRaff + 50 μg ml⁻¹ Pronase E (Sigma-Aldrich, 1074330001). Cells were resuspended in YPRaff medium containing 100 μg ml⁻¹ Pronase E with 5 μg ml⁻¹ nocodazole for 3 h. Cells were then divided into two and 2% of glucose or galactose was added, respectively, to induce Cdc6ΔNT for 3 h in the presence of galactose only. Cells were collected and lysed with lysis buffer (2% Triton, 1% SDS, 100 mM NaCl, 10 mM Tris pH 8.0, 1 mM EDTA and protease inhibitor (AEBSF, Leupeptin, Pepstatin A)). Glass beads and phenol/chloroform were added together and tubes were vortexed for 1 min. The supernatant was treated with RNases at 25 °C for 30 min and then extracted with phenol/chloroform and ethanol-precipitated. The DNA was used in qPCR. A total of 9 μl of qPCR reaction was set up in 384-well plates with 4.5 μl of 2× FastStart Universal SYBR Green Master mix ROX (Roche), -0.28 μM of primers (set 1: CTL141 + CTL142 for re-replication region; set 2: CTL143 + CTL144 for internal control) for 10 min at 95 °C and then 40 cycles of 10 s at 95 °C and 30 s at 60 °C. Each DNA sample was first evaluated for the linearity of PCR by performing serial dilutions. The fold change of threshold cycle (Ct) was determined using the 2^{-ΔΔCt} method⁴⁹, where ΔΔCt = (Ct_{re-replication region} - Ct_{internal control})_{galactose} - (Ct_{re-replication region} - Ct_{internal control})_{glucose}.

Nucleosome-flanked origins

Nucleosome-flanked origins of replication were prepared with purified yeast histone octamers as previously described¹¹ on the DNA substrates of N-ARS1-N or N-90bp-N. Plasmids containing N-ARS1-N and N-90bp-N were synthesized by Eurofins and used as a template for PCR to produce linear DNA substrates using the primers NCPF and NCP R. Origin substrates were amplified using standard PCR protocols and were purified by anion exchange chromatography using a 1 ml RESOURCE Q column (GE Healthcare). Peak fractions were ethanol-precipitated and resuspended in TE buffer.

Nucleosome assembly

Purified origin DNA substrates were combined with soluble histone octamers to form nucleosomes by salt deposition^{11,50}. Nucleosome reconstitution was optimized in small-scale titrations, and the products were checked by 4% native PAGE.

Negative-stain EM MCM loading assays

MCM loading experiments, negative-stain sample preparation, imaging and analysis were carried out as previously described¹¹, with minor modifications (see below).

Sample preparation

Nucleosome-flanked ARS1/90 bp origin substrates (7.5 nM) were incubated with WT or mutant ORC (20 nM), Cdc6 (20 nM) and MCM-Cdt1 (40 nM) with mixing (1,250 rpm) in EM buffer (25 mM HEPES pH 7.6, 10 mM MgOAc, 100 mM NaOAc, 0.02% NP-40, 80 mM KCl, 1 mM DTT, 5% glycerol) and 2 mM ATP in a final reaction volume of 20 μl. In experiments testing CDK-phosphorylated ORC, ORC was pre-phosphorylated for 10 min before Sic1 was added for 5 min to inhibit further CDK activity. Negative-stain grids were prepared after 2 min (MO detection) and 10 min (DH detection) incubation at 24 °C. In all cases, samples were diluted fivefold before making grids.

Grid preparation

Samples were applied to glow-discharged 300-mesh copper grids with carbon film (EM Resolutions). A 3 μl aliquot of sample was applied to each grid and incubated for 1 min. Staining was performed with four

drops of 40 μ l 2% uranyl acetate, and the grids were blotted to remove excess stain.

Data collection

Micrographs were collected on a Tecnai LaB6 G² Spirit transmission electron microscope (FEI) operating at 120 keV, with a 2K \times 2K GATAN Ultrascan 100 camera. Images were recorded at a nominal magnification of 30K (3.45 Å pixel size) and a defocus range of -0.5–2 μ m.

Image processing

All datasets were processed in Relion (v.3.1)⁵¹ using a common processing pipeline. The contrast transfer function (CTF) of each micrograph was estimated using Gctf (v.1.06)⁵². Particles were picked with Topaz⁵³ using a model that had been pre-trained to pick MCM-Cdt1, ORCs, MOs and MCM-DHs in negative-stain EM data. Particles were initially extracted with a 128-pixel box, rescaled to 64 pixels and subjected to two rounds of reference-free 2D classification. All MCM-containing particles were re-extracted with a 128-pixel box without rescaling. The particles were subjected to a further round of 2D classification. From this classification, particles that contributed to classes containing the MO and DH intermediates were selected and further classified, as required. Finally, particles contributing to classes that contained an MCM (total MCMs, MOs and DHs) were quantified from the appropriate 2D classification. The proportion of MCM-containing particles contributing to each intermediate state was plotted using Prism.

ReconSil

Datasets for ReconSil images were processed together in Relion (v.3.1)⁵¹. CTF estimation was performed using Gctf (v.1.06)⁵². Particles were picked with Topaz⁵³ using models pre-trained to pick MCM-containing particles (as above), ORCs and nucleosomes. Particle picks were combined, duplicates removed and extracted particles were subjected to multiple rounds of reference-free 2D classification. ReconSil micrographs were generated using the command-line tool 'relion_particle_reposition' in Relion (v.3.1) to overlay particles in the raw micrographs with the 2D averages that those particles contributed to. Individual origins were extracted from raw and ReconSil micrographs (320-pixel box size). Representative examples were selected from fully reconstituted origins where confident assignment of co-localization to the same origin could be made (as previously described¹¹).

Cryo-EM of DNA-bound SHs and DHs loaded by ORC phosphorylated on Orc2

Image acquisition, refinement and validation statistics for the SH and DH structures below can be found in Table 1.

Sample preparation

Samples were prepared as described above for the negative-stain EM experiments with the following modifications:

Mutant ORC (Orc6-4A; 40 nM) was phosphorylated by CDK (10 nM) for 10 min in CDK buffer (25 mM HEPES pH 7.6, 10 mM MgOAc, 100 mM NaOAc, 80 mM KCl, 1 mM DTT, 2 mM ATP), before Sic1 (30 nM) was added to inhibit further CDK activity. Nucleosome-flanked ARS1 origin substrates (15 nM) were incubated with pre-phosphorylated Orc6-4A mix (as above), Cdc6 (40 nM) and MCM-Cdt1 (80 nM), with mixing (1,250 rpm) in cryo-EM buffer (25 mM HEPES pH 7.6, 10 mM MgOAc, 100 mM NaOAc, 80 mM KCl, 1 mM DTT) and 2.2 mM ATP in a final reaction volume of 50 μ l. The reaction was incubated at 30 °C for 30 min before being used to prepare cryo-EM grids. Next, 4 μ l of sample was applied to fresh graphene-oxide coated 300-mesh UltrAuFoil R1.2/1.3 grids⁵⁴ and incubated for 30 s before vitrification using a Vitrobot Mark IV (Thermo Fisher) cooled to 10 °C with 100% humidity. Grids were blotted for 5 s and plunged into liquid ethane.

Cryo-EM data collection

Data were collected on a Titan Krios EM equipped with a K2 Summit direct electron detector (Gatan) at the Francis Crick Institute (Structural Biology STP).

Cryo-EM image processing

SH and DH. Image processing was performed in RELION (v.3.1)⁵¹ (Extended Data Figs. 8 & 9). Movie stacks were aligned and motion-corrected using MotionCor2 (ref. 55), retaining all frames. The CTF of each micrograph was estimated using Gctf v1.06 (ref. 52). Particles were automatically picked using Topaz⁵³. First, particles were picked using a general Topaz model (scale factor, 4; model, resnet8_u32; radius, 20). These particles were extracted (320-pixel box, rescaled to 80 pixels) and subjected to multiple rounds of reference-free 2D classification to isolate SH and DH particles for subsequent processing.

High-quality DH particles were subjected to iterative rounds of 3D refinement, particle polishing (including increasing the box size to 420 pixels), CTF refinement and a final round of 2D classification, yielding the final EM map at an average resolution of 2.8 Å, reconstructed from 135,143 MCM-DH particles. The final RELION map was subject to density modification using resolve_cryo_em in Phenix 1.19.2 (ref. 56) to generate a 2.6 Å map used for model building (Extended Data Fig. 5).

SH particles obtained from 2D classification were used for Topaz training (scale factor, 4; cnn_model, resnet8; radius, 3). SH particles were picked using the new Topaz model (selection threshold, -2), extracted (280-pixel box, rescaled to 70 pixels) and subjected to two rounds of reference-free 2D classification. SH particles were re-extracted (280-pixel box, unbinned) and classified into three classes using a 30 Å filtered reference from an ab initio reconstruction in CryoSPARC⁵⁷. High-quality SH particles were subjected to iterative rounds of particle polishing (including increasing the box size to 420 pixels), CTF refinement, masked 3D refinement and a final round of 2D classification (without alignment), yielding the final EM map at an average resolution of 3.4 Å, reconstructed from 396,366 SH particles. The final RELION map was subject to density modification using resolve_cryo_em in Phenix 1.19.2 (ref. 56) to generate a 3.1 Å map used for model building (Extended Data Fig. 5).

Molecular modeling

DH. Molecular modeling of the DH complex was performed using a density-modified map generated using resolve_cryo_em. A published DH model (PDB 7P30)⁵⁸ was used as an initial model and rigid-body docked into the new DH EM map. The resulting model was subject to manual modification in Coot⁵⁹ and real-space refinement in Phenix 1.19.2 (ref. 60). All figures were generated using UCSF ChimeraX⁶¹.

SH. Molecular modeling of the SH complex was performed using a density-modified map generated using resolve_cryo_em. An initial model of a loaded SH was extracted from the higher-resolution DH model (this study) and rigid-body docked into the SH EM map. The resulting model was subject to iterative rounds of manual modification in Coot⁵⁹ and real-space refinement in Phenix 1.19.2 (ref. 60). All figures were generated using UCSF ChimeraX⁶¹.

Orc2 IDR AlphaFold2 modeling

The MO interaction interface, consisting of *Saccharomyces cerevisiae* Orc2 (P32833), Orc3 (p54790), Orc5 (P50874, amino acids 319–479), Orc6 (P38826), Mcm2 (P29469, amino acids 178–457), Mcm5 (P29496, amino acids 1–336) and Mcm6 (P53091, amino acids 88–463), was modeled using AlphaFold2 (2.3.1)¹⁴ implemented in AlphaFold2 (0.30.0)⁶². The five resulting models positioned the Orc2 IDR amino acids 190–231 in the same location, wrapping around the Orc6 TFIIB-B domain. Orc3 (amino acids 270–419) in the top-ranked model was aligned with the corresponding sequence in the previously determined MO structure (PDB 6RQC)¹¹ using the matchmaker tool in ChimeraX

(v.1.6)⁶⁰. The Orc2 IDR (amino acids 190–231) was fit as a rigid body into the previously unassigned density in the MO map using the ‘Fit in Map’ tool in ChimeraX. The entire MO model, with the Orc2 IDR, was subjected to a single round of real-space refinement in Phenix (v.1.21.2)⁶⁰. Figure 1c and Extended Data Fig. 1 (AlphaFold2 figure) display EMready⁴⁵ density-modified EM maps obtained from the multi-body refinement of the MO intermediate. Similar AlphaFold2 predictions of the ORC subunits alone, or the ORC subunits with the complete N-terminal domains of Mcm2–7, yielded almost identical predictions for the interaction of the Orc2 IDR with Orc6.

Cryo-EM of MO formation assays on 90 bp synthetic origins

Sample preparation. Samples were prepared as described above for the cryo-EM experiments with the following modifications:

Nucleosome-flanked 90 bp origin substrates (15 nM) were incubated with WT ORC or Orc2ΔN (40 nM), Cdc6 (40 nM) and MCM–Cdt1 (80 nM), with mixing (1,250 rpm) in cryo-EM buffer (25 mM HEPES pH 7.6, 10 mM MgOAc, 100 mM NaOAc, 80 mM KCl, 1 mM DTT) and 2.2 mM ATP in a final reaction volume of 20 μl. The reaction was incubated at 24 °C for 2 min before cryo-EM grid preparation. Then, 4 μl of sample was applied to fresh graphene-oxide-coated 300-mesh UltraAuFoil R1.2/L3 grids⁵⁴ and incubated for 30 s before vitrification using a Vitrobot Mark IV (Thermo Fisher) cooled to 10 °C with 100% humidity. Grids were blotted for 5 s and plunged into liquid ethane.

Cryo-EM data collection

Data were collected at the Francis Crick Institute (Structural Biology STP) on a 300 kV Titan Krios electron microscope equipped with a Falcon4i direct electron detector (Thermo Fisher Scientific). Movies were recorded at a magnification of ×130,000 (pixel size, 1.08 Å) with an electron exposure (e⁻ Å⁻²) of 32.5 and a defocus range of 1–5 μm. In total, 24,315 movies were collected for the Orc2ΔN dataset and 21,370 for the WT ORC dataset.

Cryo-EM image processing

Movie stacks were aligned and motion-corrected using MotionCor2 (ref. 55), retaining all frames. All downstream processing was performed in CryoSPARC (v.4.4.0). The CTF of each micrograph was estimated using Patch CTF estimation. Particles were automatically picked using the Blob Picker using the default parameters (minimum/maximum particle diameters, 150 Å/250 Å; minimum separation distance, 0.7). Micrographs with a poor CTF fit, no graphene oxide (empty holes) or ice contamination were removed, yielding final micrograph stacks of 18,414 micrographs (Orc2ΔN) and 18,156 (WT ORC). Particles were initially extracted (560-pixel box, rescaled to 140 pixels) and subjected to multiple rounds of reference-free 2D classification to isolate MCM-containing particles. A class depicting the MCM single hexamer was selected and used for subsequent Template Picking (particle diameter, 200 Å), and extracted particles were subjected to reference-free 2D classification, as above. MCM-containing particle stacks from the Blob and Template pickers were merged and duplicate particles removed before final 2D classifications with unbinned particles (560-pixel box).

High-quality DH particles were additionally subjected to Ab Initio 3D reconstruction and non-uniform 3D refinement⁶³, yielding EM maps at average resolutions of 2.96 Å (WT ORC) and 3.08 Å (Orc2ΔN), reconstructed from 149,543 and 137,314 MCM-DH particles, respectively.

Simulating MCM-DH formation efficiency from two diffusing MCM-SHs

We model the separation-dependent MCM-DH formation efficiency using stochastic simulations of one-dimensional diffusion of MCM-SHs sliding along the DNA. MCM-DH formation efficiency is computed from the probability of collision of two diffusing MCM-SHs given by the intersection of their diffusion trajectories. The simulation consists

of four key steps: MCM-SH loading, MCM-SH diffusion, MCM-SH dissociation and MCM-DH formation.

MCM-SH loading. The simulation takes place on a DNA substrate consisting of two origin sequences in a head-to-head orientation, with the 5' ends of the ORC binding site pointed towards each other. The separation between the two origins is defined as the distance between their 5' ends of the ORC binding sites, as shown in Extended Data Fig. 7b. ORC binds to an origin sequence with an overhang of 6 bp ahead of the ORC binding site^{15,64} (Extended Data Fig. 7c). This ORC complex can then load an MCM-SH ahead of itself, which occupies 35 bp on the DNA substrate⁶⁵. This implies that the loading of one MCM-SH complex onto the DNA occupies at least 41 bp (6 bp ORC overhang + 35 bp MCM-SH) past the origin on the DNA substrate. The simulation is initialized with both ORC sites loaded with MCM-SHs with N-termini pointing towards each other.

MCM-SH diffusion. Given that MCM-SH sliding is independent of ATP hydrolysis, we assume that its diffusion occurs at thermal equilibrium and is therefore not driven by the input of external energy. In such conditions, the displacement of MCM-SH per unit time follows a Gaussian distribution given by:

$$P(x, \Delta t) = \frac{1}{\sqrt{4\pi D\Delta t}} e^{-\frac{(x-x_0)^2}{4D\Delta t}} \quad (1)$$

where x is the position of the MCM-SH, D is the diffusion coefficient, Δt is the duration of the time step and x_0 is the initial position. After initialization of the simulation, the displacement of MCM-SH in the following time step is determined by sampling this probability distribution using the value of MCM-SH diffusion constants measured from single-molecule fluorescence tracking experiments^{31,32}.

$$x_{n+1} = x_n + P(x, \Delta t) \quad (2)$$

$$x_{n+1} = x_n + \sqrt{2D\Delta t} \times \text{randn}() \quad (3)$$

where ‘randn()’ is the MATLAB function to generate normally distributed random numbers. The time step of the simulation is chosen such that the mean squared displacement (MSD) of MCM-SH for the given value of diffusion constant is less than 1 bp of the DNA.

$$\text{MSD} = \langle (x(\Delta t) - x_0)^2 \rangle = 2D\Delta t \quad (4)$$

Thus, the time step of the simulation was chosen to be 10 μs.

MCM-SH dissociation from the DNA. Once loaded onto the DNA substrate, MCM-SHs dissociate from the DNA with an experimentally measured half-life of 3 min (Fig. 5b). We implement this phenomenon in our simulations by assigning a dissociation probability to each loaded MCM-SH onto the DNA. The dissociation probability is computed using the exponential distribution that satisfies the experimentally measured half-life:

$$\tau_{\text{MCM-SH}} = -\frac{\tau_{\text{MCM-SH}}^{1/2}}{\log_e(0.5)} \quad (5)$$

$$P_{\text{dissociation}} = \frac{1}{\tau_{\text{MCM-SH}}} e^{-\frac{t}{\tau_{\text{MCM-SH}}}} \quad (6)$$

where $\tau_{\text{MCM-SH}}^{1/2}$ is the experimentally measured MCM-SH half-life and t is the total time spent by MCM-SH on the DNA since its loading. At every time step, a random number, R , is sampled from a uniform distribution using the MATLAB function rand(). If R is smaller than $P_{\text{dissociation}}$, the

corresponding MCM-SH is said to be dissociated from the DNA, and the simulation is stopped as MCM-DH formation is no longer possible.

MCM-DH formation. To successfully form an MCM-DH, the two loaded MCM-SHs must collide with each other while diffusing along the DNA. We define a collision event as the first instance when the distance between the N-termini of both MCM-SHs is ≤ 0 bp during the simulation. The time duration from the start of the simulation to the time step corresponding to the collision event is referred to as the collision time, which also corresponds to the first-passage time of the collision process. The probability of MCM-DH formation is thus the probability of collision of two MCM-SHs loaded onto the DNA, which depends on the separation between the ORC binding sites, the availability of the binding site on the DNA for the second MCM-SH, the diffusion constants of the MCM-SHs, the half-life of MCM-SH on the DNA and the total time for the simulation.

Simulation results. The diffusion coefficient of MCM onto the DNA has been observed to be $800 \pm 200 \text{ bp}^2 \text{ s}^{-1}$ from single-molecule fluorescence tracking experiments³². The half-life of MCM-SH on the DNA is measured to be 3 min (Fig. 5b). Using these values as our simulation parameters, we quantify the dynamics of MCM-DH formation as a function of the separation between the ORC loading sites as follows. For each case of separation, we first quantify the number of simulated trajectories that contain a collision event between two MCM-SHs and measure the time between the start of the simulation to the collision event, hereafter referred to as collision time (t_c) Extended Data Fig. 7b. The probability distribution of collision times, $P(t_c)$, is generated from all the iterations (Extended Data Fig. 7c). The cumulative sum of this distribution, given by $C(t) = \sum_{t_c=0}^t P(t_c)$, refers to the probability of collisions occurring before time t , which is, by definition, the probability of MCM-DH formation within time t (Extended Data Fig. 7d). Computing $C(t)$ for various separations between ORC binding sites at a fixed time (20 min) determined by the incubation time in bulk experiments (Fig. 5d) allows us to compare the relative MCM-DH formation efficiencies on the corresponding DNA substrates (Extended Data Fig. 7e).

We observe that the relative MCM-DH formation efficiency has a maximum at separation of 82 bp between the ORC binding sites, which corresponds to the case when MCM-SHs are loaded closest to each other onto the DNA (ORC overhang + MCM-SH + MCM-SH + ORC overhang = $6 + 35 + 35 + 6 = 82$ bp). At separations greater than 82 bp, the MCM-DH formation efficiency decreases with increasing separation (and shows a good agreement with exponential trend) as both MCM-SHs loaded onto the DNA must diffuse along the DNA and collide with each other before either or both of them dissociate from the DNA.

Reporting summary

Further information on research design is available in the Nature Portfolio Reporting Summary linked to this article.

Data availability

The data supporting this study are available within the paper, its Supplementary Information and Source Data files. Atomic model coordinates and cryo-EM maps have been deposited in the PDB and Electron Microscopy Data Bank (EMDB), under accession codes PDB [8R1F](#) and EMD-[19186](#) (DH), PDB [8R1G](#) and EMD-[19187](#) (SH) and PDB [9J3I](#) (MO with Orc2 IDR). Access to unprocessed electron microscopy datasets can be provided by the corresponding author upon reasonable request. Source data are provided with this paper.

References

- Cameron, G. et al. Sister chromatid cohesion establishment during DNA replication termination. *Science* **384**, 119–124 (2024).
- Drury, L. S. & Diffley, J. F. X. Factors affecting the diversity of DNA replication licensing control in eukaryotes. *Curr. Biol.* **19**, 530–535 (2009).

- Schmittgen, T. D. et al. Quantitative reverse transcription-polymerase chain reaction to study mRNA decay: comparison of endpoint and real-time methods. *Anal. Biochem.* **285**, 194–204 (2000).
- Luger, K., Rechsteiner, T. J. & Richmond, T. J. Preparation of nucleosome core particle from recombinant histones. *Methods Enzymol.* **304**, 3–19 (1999).
- Zivanov, J., Nakane, T. & Scheres, S. H. W. Estimation of high-order aberrations and anisotropic magnification from cryo-EM data sets in RELION-3.1. *IUCr* **7**, 253–267 (2020).
- Zhang, K. Gctf: real-time CTF determination and correction. *J. Struct. Biol.* **193**, 1–12 (2016).
- Bepler, T. et al. Positive-unlabeled convolutional neural networks for particle picking in cryo-electron micrographs. *Nat. Methods* **16**, 1153–1160 (2019).
- Martin, T. G., Boland, A., Fitzpatrick, A. W. P. & Scheres, S. H. W. Graphene oxide grid preparation. *Figshare* <https://doi.org/10.6084/m9.figshare.3178669.v1> (2016).
- Zheng, S. Q. et al. MotionCor2: anisotropic correction of beam-induced motion for improved cryo-electron microscopy. *Nat. Methods* **14**, 331–332 (2017).
- Terwilliger, T. C., Ludtke, S. J., Read, R. J., Adams, P. D. & Afonine, P. V. Improvement of cryo-EM maps by density modification. *Nat. Methods* **17**, 923–927 (2020).
- Punjani, A., Rubinstein, J. L., Fleet, D. J. & Brubaker, M. A. cryoSPARC: algorithms for rapid unsupervised cryo-EM structure determination. *Nat. Methods* **14**, 290–296 (2017).
- Greiwe, J. F. et al. Structural mechanism for the selective phosphorylation of DNA-loaded MCM double hexamers by the Dbf4-dependent kinase. *Nat. Struct. Mol. Biol.* **29**, 10–20 (2022).
- Casanal, A., Lohkamp, B. & Emsley, P. Current developments in Coot for macromolecular model building of electron cryo-microscopy and crystallographic data. *Protein Sci.* **29**, 1069–1078 (2020).
- Afonine, P. V. et al. Real-space refinement in PHENIX for cryo-EM and crystallography. *Acta Crystallogr. D Struct. Biol.* **74**, 531–544 (2018).
- Pettersen, E. F. et al. UCSF ChimeraX: structure visualization for researchers, educators, and developers. *Protein Sci.* **30**, 70–82 (2021).
- Yu, D., Chojnowski, G., Rosenthal, M. & Kosinski, J. AlphaPulldown—a Python package for protein–protein interaction screens using AlphaFold-Multimer. *Bioinformatics* <https://doi.org/10.1093/bioinformatics/btac749> (2023).
- Punjani, A., Zhang, H. & Fleet, D. J. Non-uniform refinement: adaptive regularization improves single-particle cryo-EM reconstruction. *Nat. Methods* **17**, 1214–1221 (2020).
- Feng, X. et al. The structure of ORC–Cdc6 on an origin DNA reveals the mechanism of ORC activation by the replication initiator Cdc6. *Nat. Commun.* **12**, 3883 (2021).
- Noguchi, Y. et al. Cryo-EM structure of Mcm2–7 double hexamer on DNA suggests a lagging-strand DNA extrusion model. *Proc. Natl Acad. Sci. USA* <https://doi.org/10.1073/pnas.1712537114> (2017).
- Baretic, D. et al. Cryo-EM structure of the fork protection complex bound to CMG at a replication fork. *Mol. Cell* **78**, 926–940.e13 (2020).

Acknowledgements

We thank A. Alidoust, N. Patel and D. Patel in the Structural Biology STP from Francis Crick Institute for yeast protein expression. We thank A. Nans, A. Purkiss and P. Walker from the Structural Biology STP for support with cryo-EM and computing. We thank G. Cameron and H. Yardimci from Francis Crick Institute for the gift of the Lac repressor protein and plasmid. We thank F. Palmero Moya of the NHD lab for discussions of simulations. This work was supported by the Francis Crick Institute, which receives its core funding from Cancer Research UK (CC2002 and CC2009), the UK Medical Research

Council (CC2002 and CC2009) and the Wellcome Trust (CC2002 and CC2009). This work was also funded by Wellcome Trust Senior Investigator Awards (106252/Z/14/Z and 219527/Z/19/Z) to J.F.X.D. and European Research Council Advanced Grants (669424-CHROMOREP and 101020432-MeChroRep) to J.F.X.D. A.C. receives funding from the European Research Council (ERC) under the European Union's Horizon 2020 Research and Innovation Program (grant agreement no. 820102). N.H.D. acknowledges funding from the Netherlands Organization for Scientific Research (NWO) through grant OCENW.M.21.173 and from a European Research Council Advanced Grant (789267-REPLICHROMA). T.C.R.M. was supported by a Novo Nordisk Fonden Hallas-Møller Emerging Investigator Grant (NNF22OC0073571), the Danish National Research Foundation (DNRF115) and the Carlsberg Foundation (CF21-0571). The funders had no role in study design, data collection and analysis, decision to publish or preparation of the manuscript. For the purpose of Open Access, the author has applied a CC BY public copyright licence to any Author Accepted Manuscript version arising from this submission.

Author contributions

C.T.L. and J.F.X.D. conceived the initial study. C.T.L. performed all biochemical MCM loading experiments, analysis of re-replication in vivo and helped with EM experiments. T.C.R.M. performed all EM experiments, image processing and atomic model building. A.C. helped with AlphaFold-multimer, cryo-EM grid preparation and screening. K.W.T. performed in vitro replication experiments. A.E. performed the EMSA experiment. P.E. performed the PWM analysis of yeast origins. S.T., H.S., C.T.L., J.F.X.D. and N.H.D. conceived

the simulation experiment, which was developed and executed by S.T. with advice from H.S. and N.H.D. C.T.L., T.C.R.M. and J.F.X.D. wrote the manuscript with input from other authors.

Funding

Open Access funding provided by The Francis Crick Institute.

Competing interests

The authors declare no competing interests.

Additional information

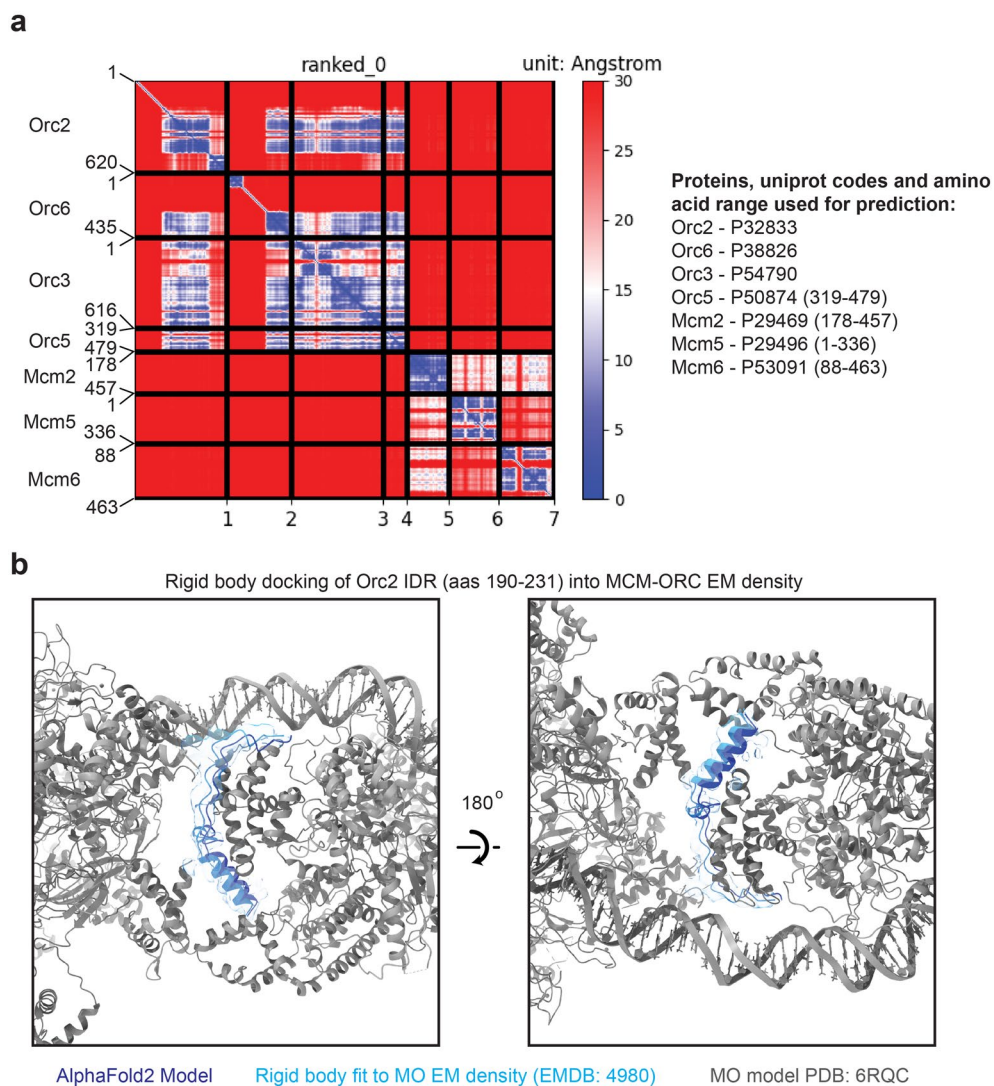
Extended data is available for this paper at <https://doi.org/10.1038/s41594-025-01591-9>.

Supplementary information The online version contains supplementary material available at <https://doi.org/10.1038/s41594-025-01591-9>.

Correspondence and requests for materials should be addressed to Thomas C. R. Miller or John F. X. Diffley.

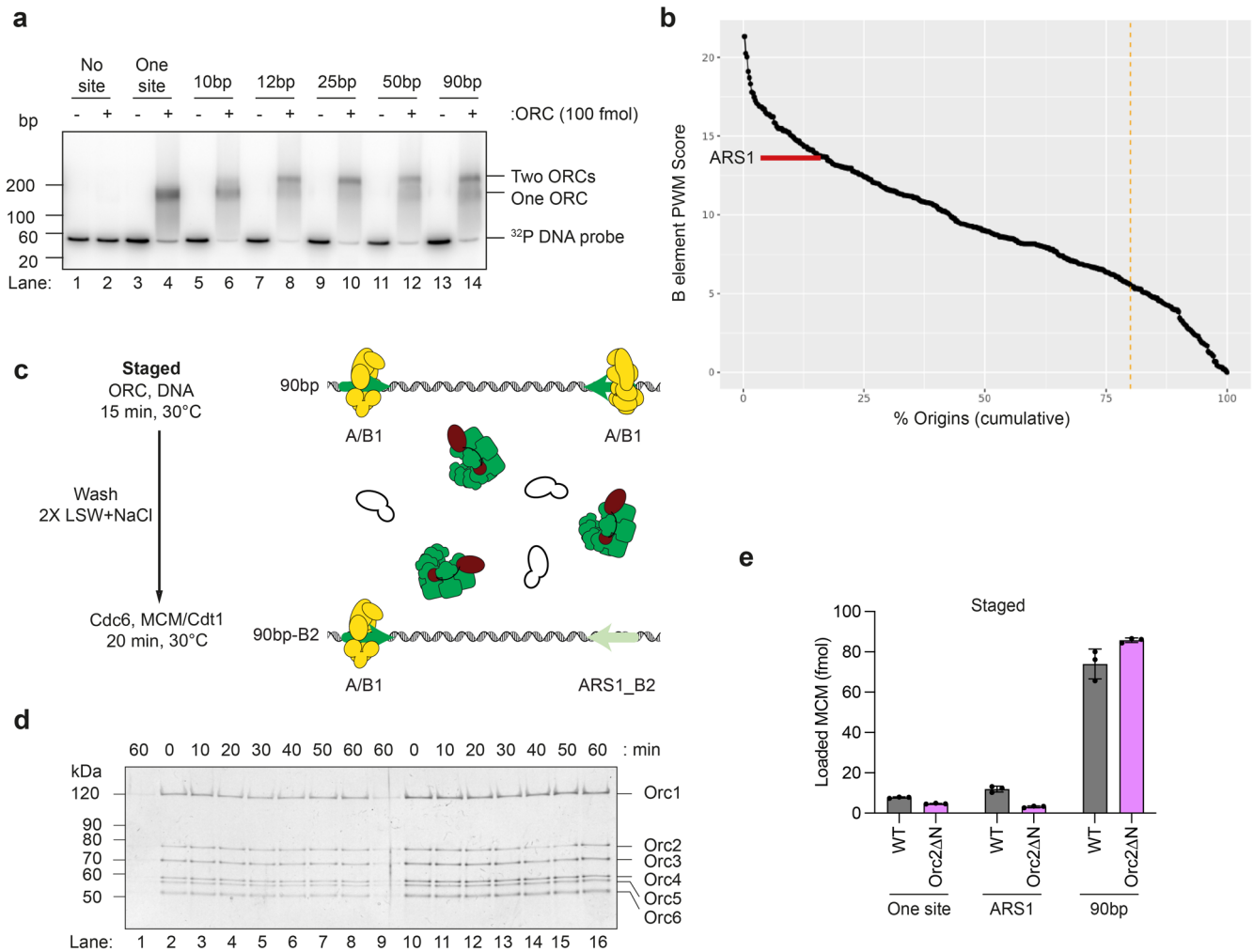
Peer review information *Nature Structural & Molecular Biology* thanks the anonymous reviewers for their contribution to the peer review of this work. Primary Handling Editor: Dimitris Typas, in collaboration with the *Nature Structural & Molecular Biology* team.

Reprints and permissions information is available at www.nature.com/reprints.



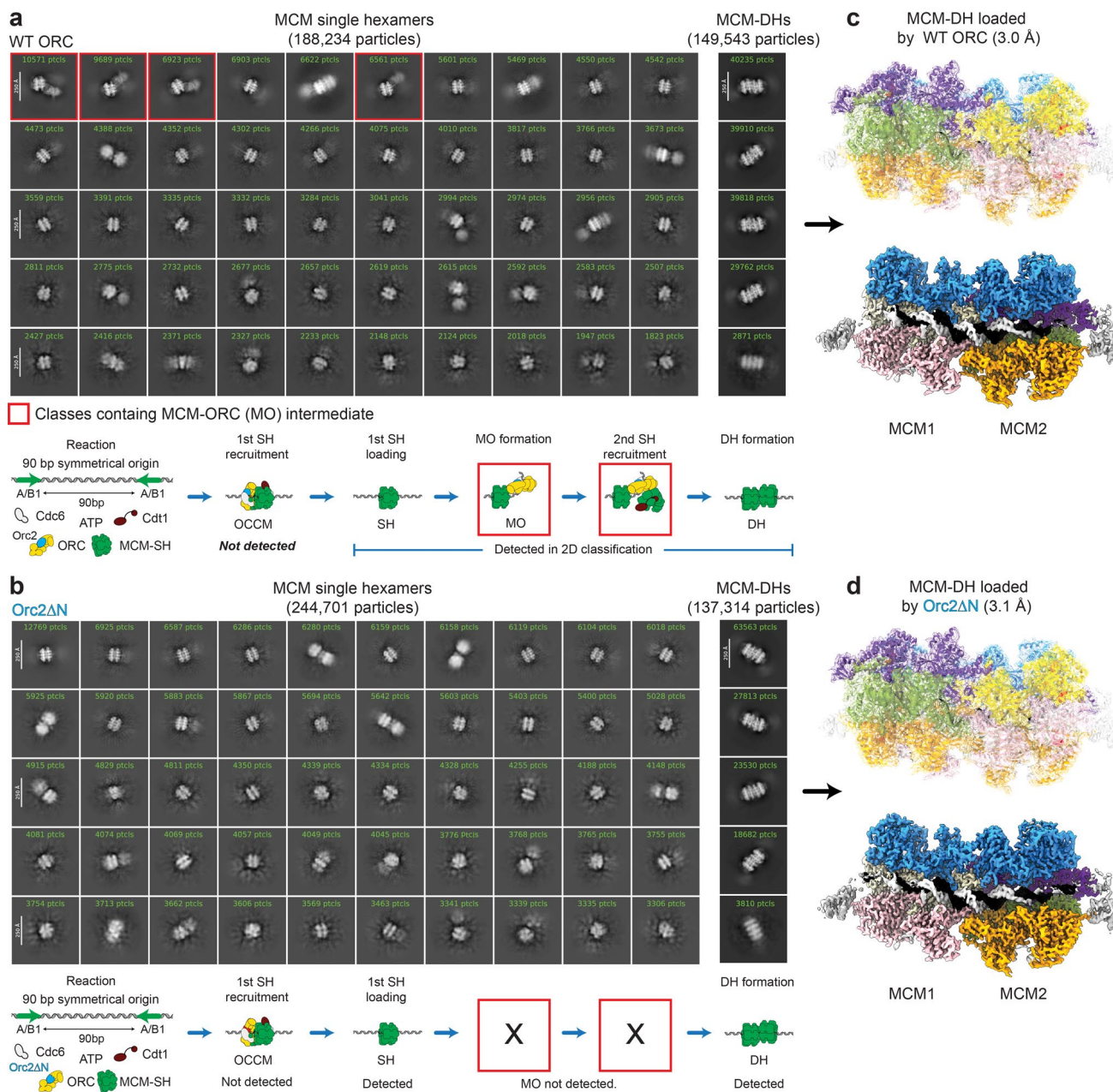
Extended Data Fig. 1 | AlphaFold2 places the Orc2 IDR at the MCM-ORC (MO) interface. **a.** Predicted aligned error (PAE) plot for the AlphaFold2 model of the MO interface in the published structure (PDB: 6RQC ref. 11). **b.** Following alignment of Orc3 (aa 270-419) in the top ranked AlphaFold2 model with the respective region of Orc3 in the MO structure, the predicted Orc2 IDR (aas 190-231) was fit as a rigid

body into previously unassigned EM density in the MO map. Here, the density displayed has been isolated from a density modified (EMready⁴⁵) map of ORC obtained from the multibody refinement of the MO (EMDB: 4980 ref. 11). The prediction places the Orc2 IDR as wrapping around the Orc6 TFIIB-B domain at the center of the MO interface.



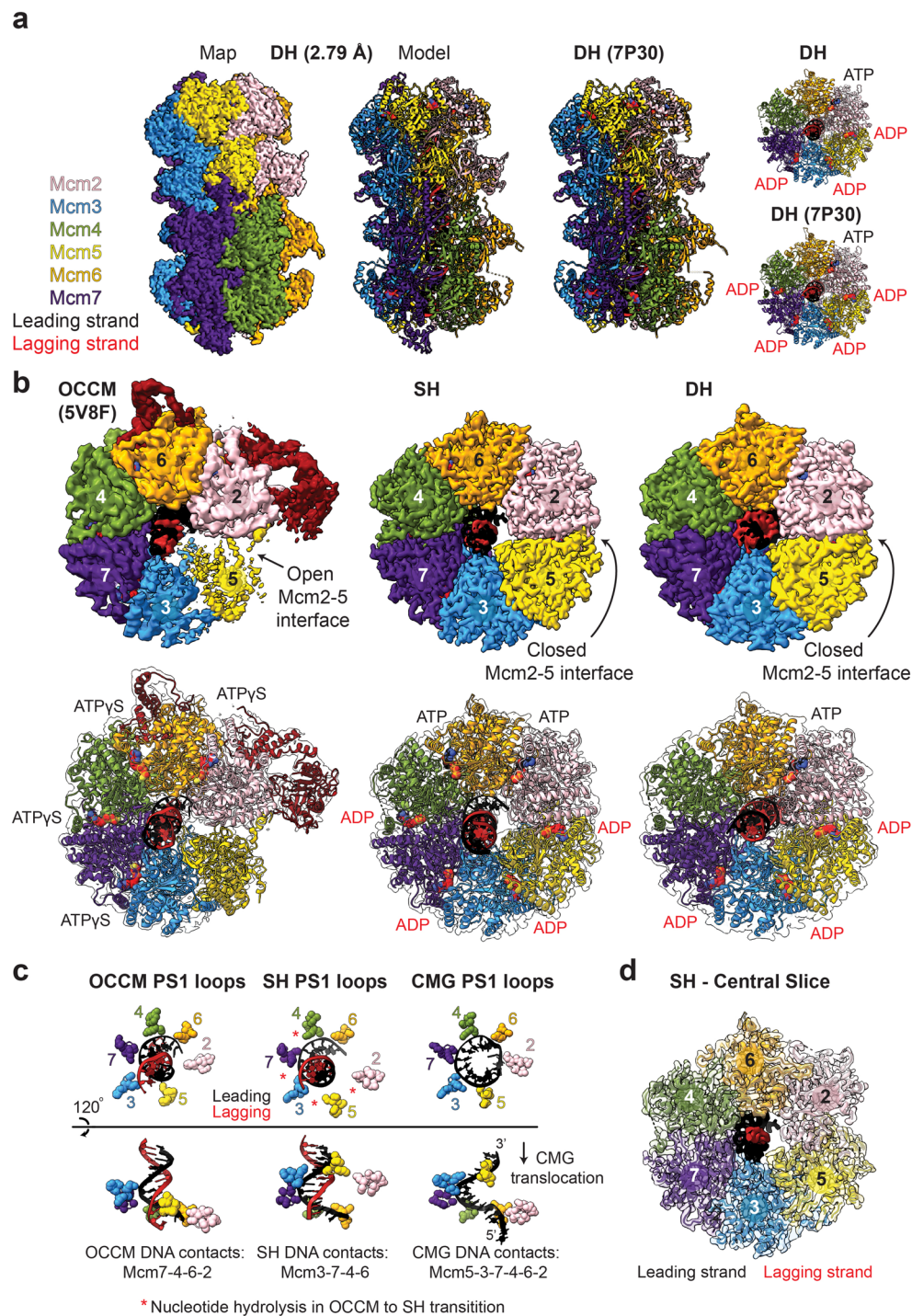
Extended Data Fig. 2 | The formation of MO stabilizes ORC binding at weak binding sites. a. EMSA of ORC binding at different distances on synthetic templates. The 10 bp distance is similar to ARS1, which can only bind a single ORC. Two ORCs can bind simultaneously on origins with a spacing of ≥ 12 bp. **b.** Approximately 15% of origins have a better match to the EACS at the weaker ORC binding site than ARS1 B2. **c.** Schematic figure of staged reaction, where ORC

only remains bound to high affinity sites after stringent washing with 150 mM NaCl. **d.** ORC remains bound to the template DNA on both 90 bp and 90bp-B2 for up to 60 min in the presence of a 50X excess of competitor DNA. In lanes 1 and 9, competitor DNA was added together with ORC during preincubation. **e.** Orc2ΔN loads MCM as efficiently as wtORC in a staged reaction. The data is plotted as mean \pm SD of three technical replicates.



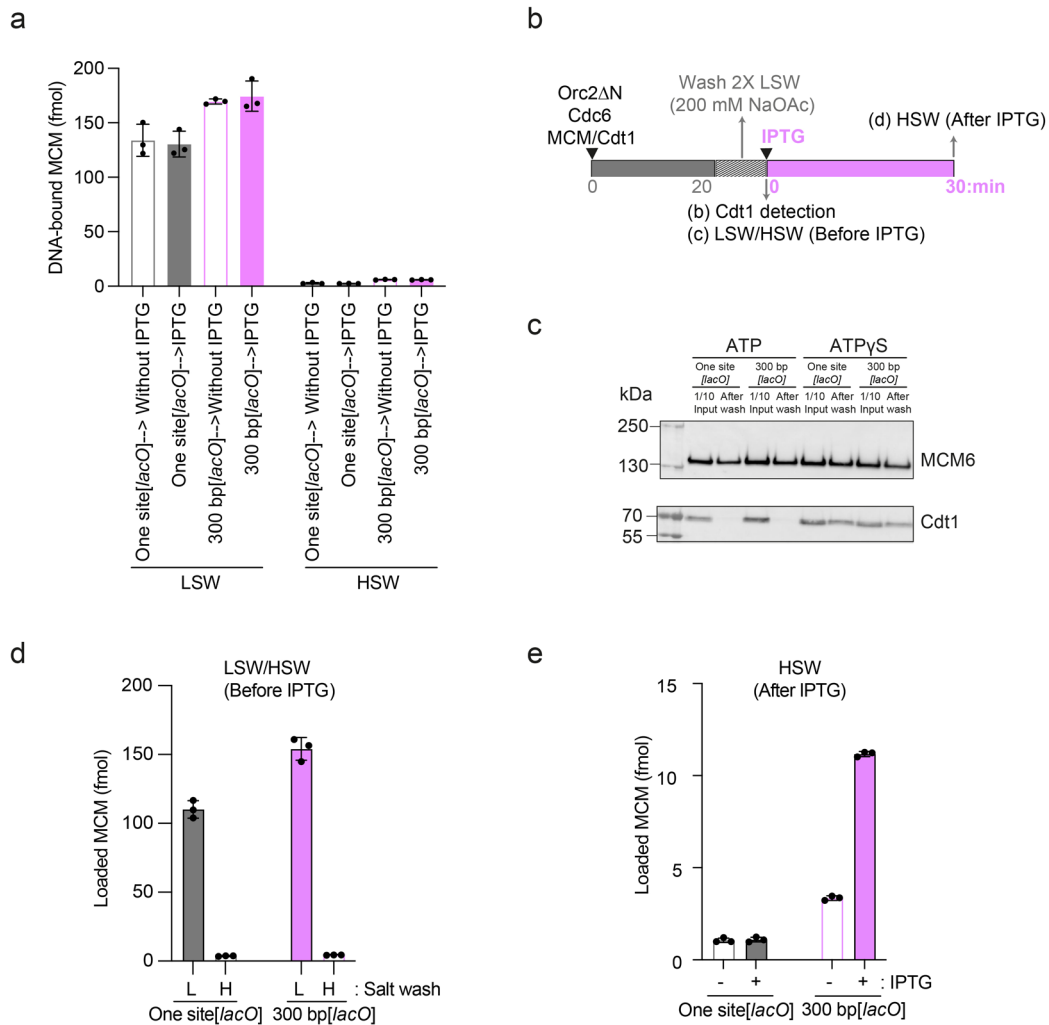
Extended Data Fig. 3 | Orc2ΔN cannot form MO intermediates on 90 bp origins containing symmetrical high-affinity ORC binding sites. 2D classification of cryo-EM particle images containing SHs and DHs loaded by wt (a) or Orc2ΔN (b). Data were collected from early time-point (2 minute) MCM loading assays designed to enrich for MO intermediates. Green numbers indicate the particles contributing to each class average. Classes containing MO or MO-like particles were not detected in the experiment containing Orc2ΔN. Cryo-EM density maps

of DHs loaded by wt (c) or Orc2ΔN (d). Top panels show EM maps with a semi-transparent surface colour zoned according to the DH atomic model described in Extended Data Fig. 5a and 10. Bottom panels show colour zoned EM maps with Mcm7,4,6 (MCM1) and Mcm2,5 (MCM2) removed to display DNA density in the DH central channel. DHs assembled on ARS1 or 90 bp symmetrical origins, with wt ORC, CDK phosphorylated ORC or Orc2ΔN all appear identical. The displayed EM density maps have been density modified using EMReady.



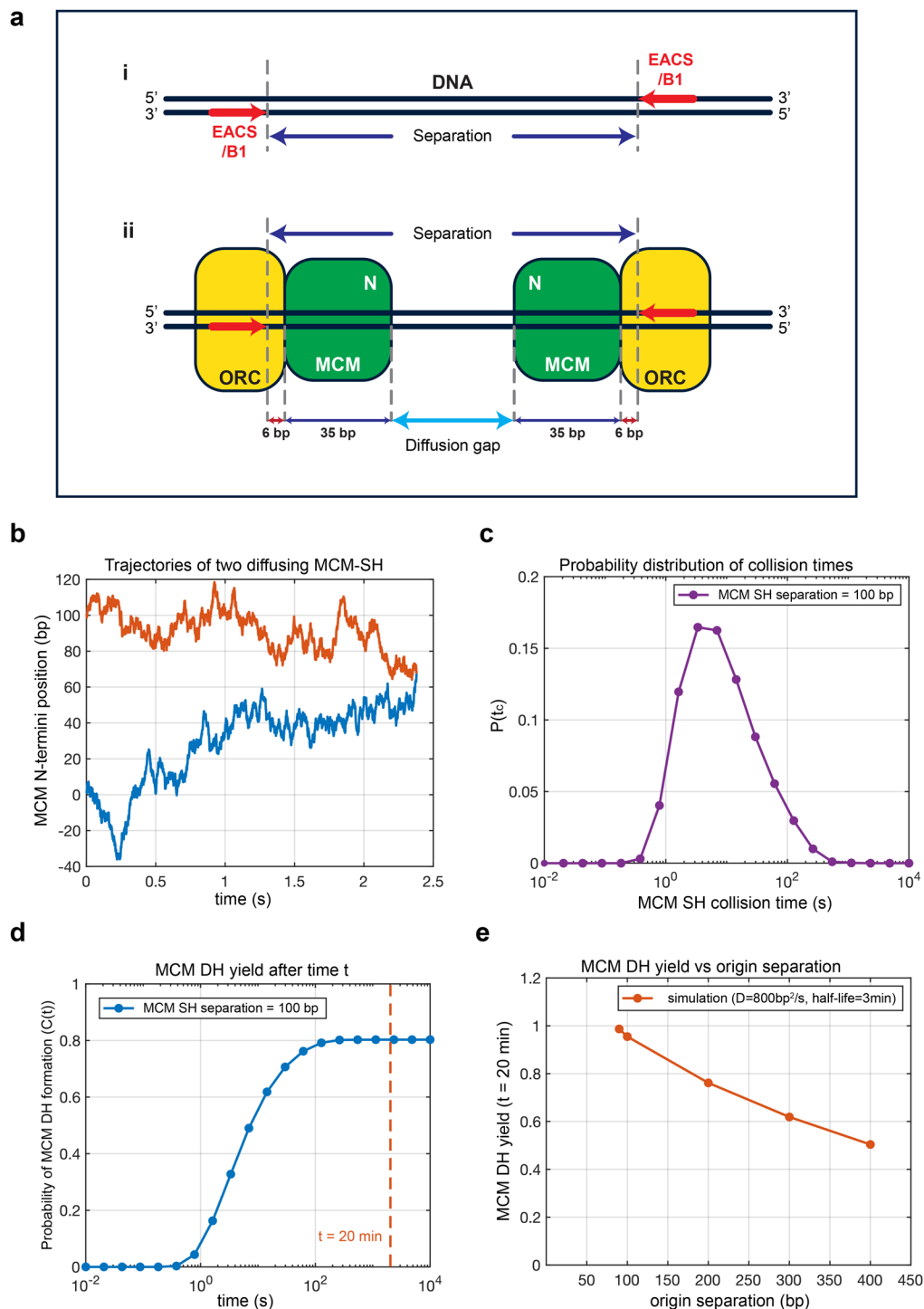
Extended Data Fig. 5 | Comparison of DHs assembled by ORC and ORC phosphorylated on Orc2. a. Cryo-EM structure and atomic model for DHs assembled by ORC phosphorylated on Orc2 (left; this study) and atomic model for DHs assembled by unphosphorylated ORC (right; PDB: 7P30 ref. 58). The DH EM density map displayed has been density modified using EMReady⁴⁵. **b.** Comparison of the MCM ring in the OCCM (left), SH (middle) and DH (right), showing that the SH and DH have fully closed Mcm2-5 interfaces and both appear

to be in post-ATP hydrolysis states relative to the OCCM. **c.** Comparison of the PS1 loops of the OCCM (5V8F⁴⁶; left), SH (this study; middle) and CMG (6SKO⁶⁶; right), showing that the SH PS1 loops adopt a staircase configuration and engage the backbone of the leading strand DNA template like the CMG. **d.** Central slice through the SH structure, highlighting the well resolved EM density for the bases in the leading strand DNA template.



Extended Data Fig. 6 | DH formation by two single hexamers independent on free MCM-Cdt1. **a.** MCM loading assay performed with 20 min incubation of Orc2ΔN, Cdc6 and MCM-Cdt1 with ATP and a DNA template containing two high affinity ORC sites separated by 300 bp and 4 *lac* operators. Aliquots taken before IPTG addition in Fig. 5d show MCM loaded onto DNA (detectable after LSW), but no HSW stable DH formation. The data is plotted as mean ± SD of three technical replicates. **b.** Schematics illustrating the assay used for MO-independent DHs formation in panel c-e. Orc2ΔN, Cdc6, MCM and Cdt1 were incubated for 20 min in the presence of LacI, then two washes with LSW (200 mM NaOAc) were introduced before the addition of IPTG to wash off free MCM-Cdt1 and Cdc6.

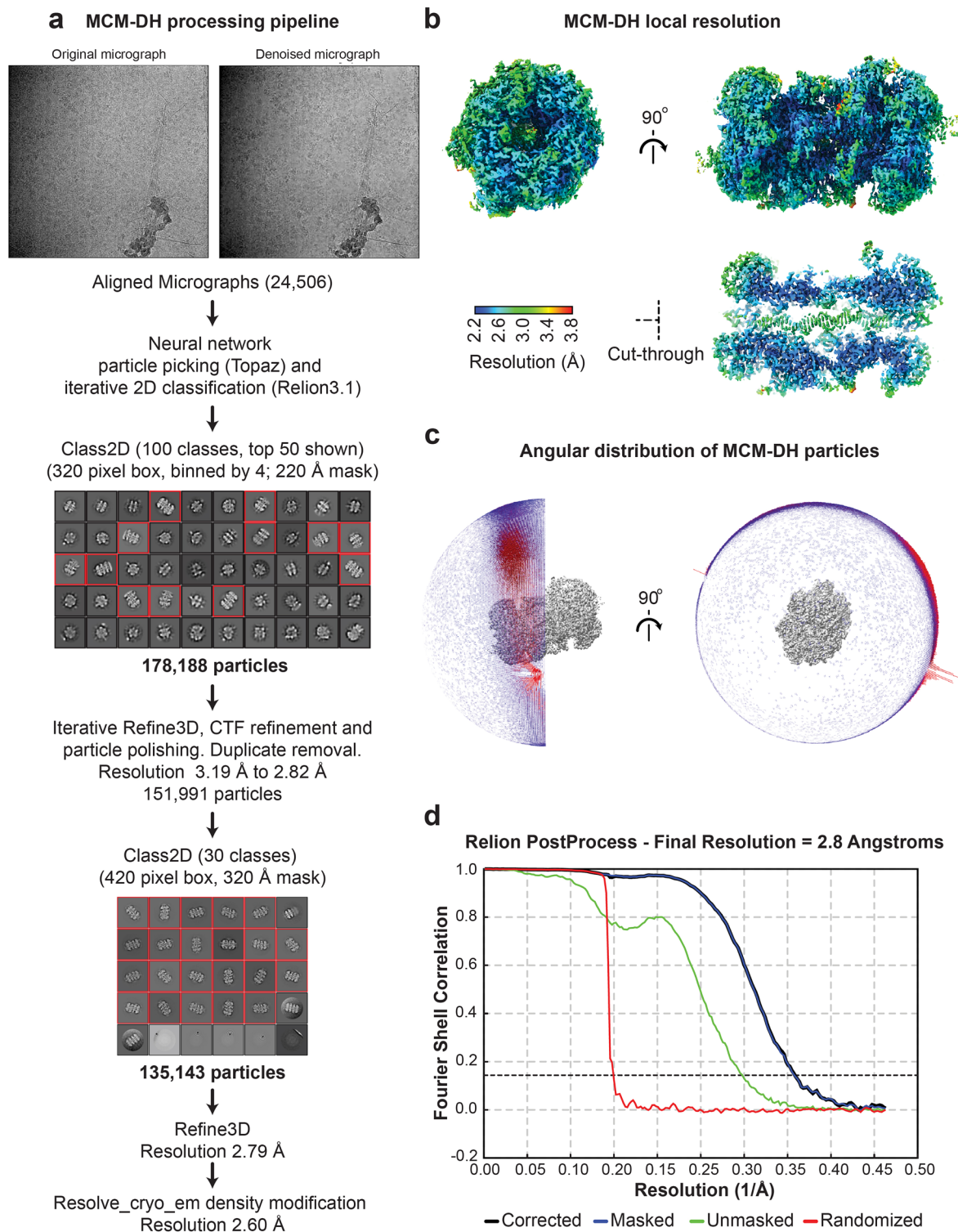
c. Aliquots were taken before IPTG addition for immunoblot detecting Cdt1, indicating that most of free MCM-Cdt1 in the solution was washed off. Mcm6 is used as a control. **d.** Aliquots were taken after extensive washes but before IPTG addition for both LSW and HSW, showing that MCM was loaded onto DNA (LSW) without forming DH (HSW). The data is plotted as mean ± SD of three technical replicates. **e.** After incubation with IPTG, the samples were washed with HSW to detect DH formation. In the presence of IPTG, approximately 3.3-fold more MCM was detected on the 300 bp [*lacO*] compared to the reaction without IPTG. The data is plotted as mean ± SD of three technical replicates.



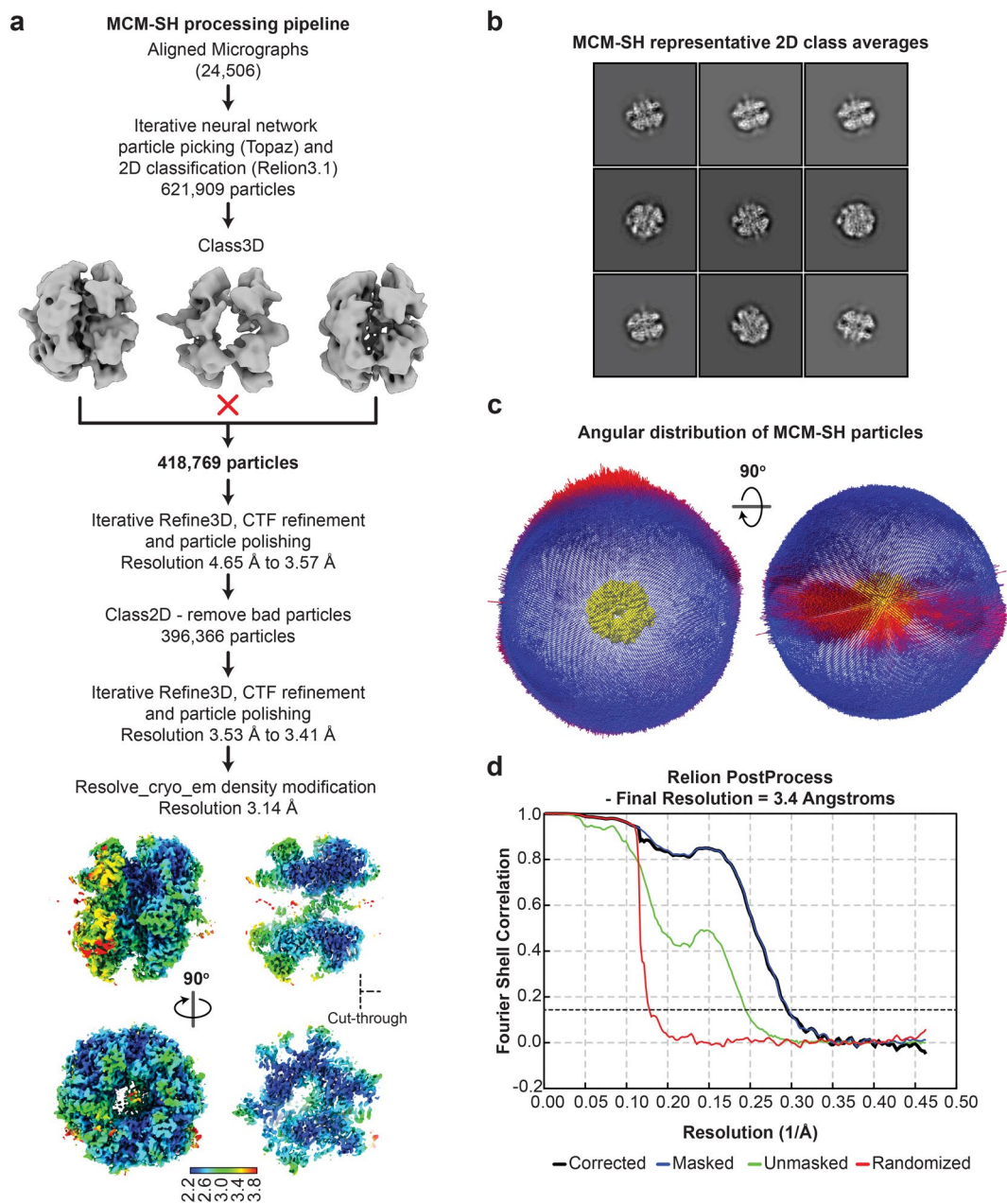
Extended Data Fig. 7 | Simulating efficiency of MCM DH formation.

a. Schematic of the simulated system and definition of relevant distances. **i.** The separation between two origins oriented towards each other on the DNA is defined as the distance in base pairs between the 5' ends of the origin sequences. **ii.** ORC binds to the origin sequence with an overhang of 6 base pairs in front of the 5' end of the origin. MCM-SH binds in front of the ORC and occupies 35 base pairs with the distance between the origin and the N-termini of MCM-SH being $6 + 35 = 41$ base pairs. The distance between the N-termini of MCM-SHs is the diffusion gap that must be overcome to result in MCM-DH formation and is determined by the separation between origin sequences and the space occupied

by ORC and MCM2-7 complexes on the DNA. **b.** An example of a simulated trace showing two MCM-SHs loaded at a separation of 100 base pairs which then diffuse along the DNA substrate and ultimately collide with each other resulting in MCM-DH formation. **c.** Probability distribution of MCM-SH collision times. **d.** Probability of MCM-DH formation with respect to time which is the cumulative sum of the MCM-SH collision time distribution shown in (c). MCM-DH yield is defined as the MCM-DH formation probability at a cutoff time determined by the incubation time in vitro experiments (in this case $t_{\text{cutoff}} = 20$ min). **e.** Simulated MCM-DH yield at various values of separation between origin sequences.



Extended Data Fig. 8 | DH cryo-EM data processing. **a.** Cryo-EM data processing pipeline for the DH. **b.** Final DHEM density map following density modification with `resolve_cryo_em`⁵⁶, coloured according to the local resolution. **c.** Angular distribution plot. **d.** Fourier shell correlation (FSC) plot obtained from Relion PostProcess.



Extended Data Fig. 9 | SH data cryo-EM processing. **a.** Cryo-EM data processing pipeline for the SH, including views of the resulting 3D density modified map coloured according to local resolution. **b.** Representative 2D classes for the SH. **c.** Angular distribution plot. **d.** Fourier shell correlation (FSC) plot obtained from Relion PostProcess.

Reporting Summary

Nature Portfolio wishes to improve the reproducibility of the work that we publish. This form provides structure for consistency and transparency in reporting. For further information on Nature Portfolio policies, see our [Editorial Policies](#) and the [Editorial Policy Checklist](#).

Statistics

For all statistical analyses, confirm that the following items are present in the figure legend, table legend, main text, or Methods section.

- | n/a | Confirmed |
|-------------------------------------|--|
| <input type="checkbox"/> | <input checked="" type="checkbox"/> The exact sample size (n) for each experimental group/condition, given as a discrete number and unit of measurement |
| <input type="checkbox"/> | <input checked="" type="checkbox"/> A statement on whether measurements were taken from distinct samples or whether the same sample was measured repeatedly |
| <input type="checkbox"/> | <input checked="" type="checkbox"/> The statistical test(s) used AND whether they are one- or two-sided
<i>Only common tests should be described solely by name; describe more complex techniques in the Methods section.</i> |
| <input checked="" type="checkbox"/> | <input type="checkbox"/> A description of all covariates tested |
| <input checked="" type="checkbox"/> | <input type="checkbox"/> A description of any assumptions or corrections, such as tests of normality and adjustment for multiple comparisons |
| <input type="checkbox"/> | <input checked="" type="checkbox"/> A full description of the statistical parameters including central tendency (e.g. means) or other basic estimates (e.g. regression coefficient) AND variation (e.g. standard deviation) or associated estimates of uncertainty (e.g. confidence intervals) |
| <input type="checkbox"/> | <input checked="" type="checkbox"/> For null hypothesis testing, the test statistic (e.g. F , t , r) with confidence intervals, effect sizes, degrees of freedom and P value noted
<i>Give P values as exact values whenever suitable.</i> |
| <input checked="" type="checkbox"/> | <input type="checkbox"/> For Bayesian analysis, information on the choice of priors and Markov chain Monte Carlo settings |
| <input checked="" type="checkbox"/> | <input type="checkbox"/> For hierarchical and complex designs, identification of the appropriate level for tests and full reporting of outcomes |
| <input checked="" type="checkbox"/> | <input type="checkbox"/> Estimates of effect sizes (e.g. Cohen's d , Pearson's r), indicating how they were calculated |

Our web collection on [statistics for biologists](#) contains articles on many of the points above.

Software and code

Policy information about [availability of computer code](#)

Data collection Typhoon phosphorimager (GE Healthcare), BMG LABTECH's Reader Control software

Data analysis Prism 10, ImageJ (Version 1.53), Snapgene (Version 8.0), Adobe Photoshop 2024

For manuscripts utilizing custom algorithms or software that are central to the research but not yet described in published literature, software must be made available to editors and reviewers. We strongly encourage code deposition in a community repository (e.g. GitHub). See the Nature Portfolio [guidelines for submitting code & software](#) for further information.

Data

Policy information about [availability of data](#)

All manuscripts must include a [data availability statement](#). This statement should provide the following information, where applicable:

- Accession codes, unique identifiers, or web links for publicly available datasets
- A description of any restrictions on data availability
- For clinical datasets or third party data, please ensure that the statement adheres to our [policy](#)

The data supporting this study are available within the paper, its Supplementary Information and Source Data files. Atomic model coordinates and cryo-EM maps have been deposited in the Protein Data Bank (PDB) and Electron Microscopy Data Bank (EMDB), under the accession codes 8RIF/EMD-19186 (DH), 8RIG/EMD-19187 (SH), and 9I3I (MO with Orc2-IDR). Access to unprocessed electron microscopy datasets can be provided by the corresponding author upon reasonable request.

Research involving human participants, their data, or biological material

Policy information about studies with [human participants or human data](#). See also policy information about [sex, gender \(identity/presentation\), and sexual orientation](#) and [race, ethnicity and racism](#).

Reporting on sex and gender	n/a
Reporting on race, ethnicity, or other socially relevant groupings	n/a
Population characteristics	n/a
Recruitment	n/a
Ethics oversight	n/a

Note that full information on the approval of the study protocol must also be provided in the manuscript.

Field-specific reporting

Please select the one below that is the best fit for your research. If you are not sure, read the appropriate sections before making your selection.

Life sciences Behavioural & social sciences Ecological, evolutionary & environmental sciences

For a reference copy of the document with all sections, see [nature.com/documents/nr-reporting-summary-flat.pdf](https://www.nature.com/documents/nr-reporting-summary-flat.pdf)

Life sciences study design

All studies must disclose on these points even when the disclosure is negative.

Sample size	Each MCM loading/recruitment assays were in triplicates for technical repeat. For in vivo-re-replication assay, three biological repeat samples were collected and repeated twice (for high and low Ct values) with triplicates. Sample sizes was determined based on statistical consideration.
Data exclusions	No data was excluded
Replication	Each MCM loading assays, recruitment assays, in vitro replication assays were individually repeated at least twice, all replicates were successful. In vivo re-replication was repeated in three biological repeats, the experiments were performed multiple times; however only complete data sets were elected due to technical issues, primarily pipetting errors, affecting result accuracy and reliability. Each negative stain EM experiment was repeated at least twice, with multiple time-points.
Randomization	Biochemical assays do not involve randomization because they follow a predefined experimental protocol where specific reagents and conditions are carefully controlled. Biochemical assays focus on precise and reproducible measurement under set conditions.
Blinding	Blinding is not applicable to biochemical assays because these experiments follow a standardized protocol.

Reporting for specific materials, systems and methods

We require information from authors about some types of materials, experimental systems and methods used in many studies. Here, indicate whether each material, system or method listed is relevant to your study. If you are not sure if a list item applies to your research, read the appropriate section before selecting a response.

Materials & experimental systems

n/a	Involvement in the study
<input type="checkbox"/>	<input checked="" type="checkbox"/> Antibodies
<input checked="" type="checkbox"/>	<input type="checkbox"/> Eukaryotic cell lines
<input checked="" type="checkbox"/>	<input type="checkbox"/> Palaeontology and archaeology
<input checked="" type="checkbox"/>	<input type="checkbox"/> Animals and other organisms
<input checked="" type="checkbox"/>	<input type="checkbox"/> Clinical data
<input checked="" type="checkbox"/>	<input type="checkbox"/> Dual use research of concern
<input checked="" type="checkbox"/>	<input type="checkbox"/> Plants

Methods

n/a	Involvement in the study
<input checked="" type="checkbox"/>	<input type="checkbox"/> ChIP-seq
<input checked="" type="checkbox"/>	<input type="checkbox"/> Flow cytometry
<input checked="" type="checkbox"/>	<input type="checkbox"/> MRI-based neuroimaging

Antibodies

Antibodies used Polyclonal antibody JDI 70, produced in rabbit against yeast Cdt1, polyclonal antibody E78, produced in rabbit against yeast Mcm6

Validation JDI 70 antibody is cited in Drury, L. S. & Diffley, J. F. X. Factors affecting the diversity of DNA replication licensing control in eukaryotes. *Curr Biol* 19, 530-535 (2009). E78 antibody data is provided in this manuscript.

Plants

Seed stocks *Report on the source of all seed stocks or other plant material used. If applicable, state the seed stock centre and catalogue number. If plant specimens were collected from the field, describe the collection location, date and sampling procedures.*

Novel plant genotypes *Describe the methods by which all novel plant genotypes were produced. This includes those generated by transgenic approaches, gene editing, chemical/radiation-based mutagenesis and hybridization. For transgenic lines, describe the transformation method, the number of independent lines analyzed and the generation upon which experiments were performed. For gene-edited lines, describe the editor used, the endogenous sequence targeted for editing, the targeting guide RNA sequence (if applicable) and how the editor was applied.*

Authentication *Describe any authentication procedures for each seed stock used or novel genotype generated. Describe any experiments used to assess the effect of a mutation and, where applicable, how potential secondary effects (e.g. second site T-DNA insertions, mosaicism, off-target gene editing) were examined.*